Master Thesis

Institute for Marine and Atmospheric research

The impact of sea level rise on tides, waves and tidal sand ridges in the North Sea

Author:
Michelle Bindels

Supervisors:
Prof. Dr. H.E. de Swart
Dr. A. Nnafie

https://www.amazingbelgium.be/2018/05/the-belgium-coastline.html

10 July, 2020

Abstract

Tidal sand ridges are large-scale bedforms that occur on continental shelves with strong tidal currents and a sandy bottom. The length of these features is in the order of several kilometres, the height in the order of tens of meters and they evolve on centennial time scales. The key objective of this study is to quantify the impact of sea level rise (SLR) on the long-term evolution of tidal sand ridges on a realistic shelf. This also requires the assessment of the changes in tidal and wind waves with a rising sea level. For this, an existing shelf model (Delft3D-SWAN) is used, and applied to model the evolution of tidal sand ridges on the Belgian continental shelf. These ridges are subject to change in mean sea level and related changes in tidal and wave forcing with time. First, the changes in tides and waves as a result of SLR are quantified through nesting of the shelf model into a larger-scale North Sea model (called DCSM-ZUNO). Second, starting from an alongshore uniform and sloping bottom, the shelf model is run in absence of SLR, until mature tidal sand ridges develop on the shelf. Finally, these ridges were used as a starting point for assessing morphodynamic changes due to SLR or differences in tidal and wind wave forcing. Different SLR scenarios were explored, using rate of SLR over the last century (2 mm/yr), the current rate of SLR (3.3 mm/yr) and different SLR rates derived from IPCC projections (3.3 mm/yr, 4.5 mm/yr, 5.4 mm/yr and 11 mm/yr).

Model results show that on the Belgian shelf a larger water depth, resulting from SLR, causes the tidal wave to travel faster and to have a larger amplitude, while the tidal current amplitudes decrease. The significant wave height and the peak wave period increase with a rising sea level, while the wave orbital velocity slightly decreases. The weakening of tidal currents and wave orbital velocities results in a decrease of sediment stirring at the bed. When imposing present-day conditions for waves and tides, the tidal sand ridges are able to keep pace with the rising sea level, even for the most extreme SLR scenario (11 mm/yr). When the effects of SLR on waves is imposed on the boundaries, the off-shore migration of the tidal sand ridges is reduced. However, the ridges are still able to keep pace with the rising sea level. Finally, when the effects of SLR on both the waves and tides are accounted for, the tidal sand ridges can keep pace with SLR, up to a SLR rate of 11 mm/yr, where the growth rate is lower than the rate of SLR.

Contents

1 Introduction

A sea shelf is an area of relatively shallow water that stretches from the coastline to the end of the continental shelf (the shelf break). The shelf break separates the sea shelf from the deep ocean. The shelf is divided into three parts, the shore (between the coastline and the water level of low tides), the inshore (with slopes in the order of $0.01 - 0.001$) and the offshore area (with slopes less than 0.001) (see Figure 1). In the shore and inshore areas, waves dominate the water motions, while tides induce changes on a times scale of several hours. In the offshore area, tides become more important, even though waves still play a role [De Swart and Yuan, 2019].

On sea shelves with a sandy bed, different bottom patterns are observed. In the shore area the distances between the crests of these patterns are in the order of 10 cm to 100 m. In the inshore area patterns can be found with a length scale up to 10 km, while in the offshore area bottom features with a length scale of up to several kilometers and a height of tens of meters can be found. The latter features will be investigated in this study, and are called tidal sand ridges (TSR). Generally, these ridges only form in the presence of medium to coarse sand and strong, asymmetric tidal currents [Dyer and Huntley, 1999]. Due to the asymmetry in the tide, the sand transport during both the ebb and flood phase is directed onto the crest [Huthnance, 1982]. Their shape is further determined by the presence of wind waves [Roos et al., 2004]. An example of TSR in the East Chinese Sea is shown in Figure 2.

Already around 40% of the world's population lives near a coastline [Bricheno and Wolf, 2018] and this is expected to grow by 58% to 71% by 2050 [Merkens et al., 2016]. Next to that, large harbours, are located near the world's coastlines. In total, 35% of the world's GDP is generated in coastal areas [Bricheno and Wolf, 2018]. It is therefore extremely important to protect these areas from storm surges and future sea level rise (SLR). Tidal sand ridges protect the coast by dissipating wave energy during storms and they are a potential source of sediment for beach nourishment [De Swart and Yuan, 2019].

The rate of SLR over the last century is measured to be 1.7 mm/yr, however this accelerated to a rate of 3.1 mm/yr in the last decade ([Pickering et al., 2012]). According to the RCP8.5 scenarios created by the Intergovernmental Panel on Climate Change (IPCC), this rate may even increase to 11 mm/yr [Church et al., 2013]. The increase in water depth will impact the behaviour of tides and waves. Previous studies have looked into the these effects. For example, Pickering et al. [2012] has studied the changes in tidal amplitude and phase of the (symmetric) M_2 tide with SLR. However, this study does not address the changes in tidal current velocities, nor are residual currents and overtides included. Both are important for sediment transport.

Amores and Marcos [2020] studied the influence of SLR on waves along global coastlines, focusing on swell waves, while Debernard and Røed [2008] investigated the future wind wave climate in the North sea. These studies provide valuable information for predicting the future wave climate, but neither of them focuses on the effects of SLR on the near bed wave orbital velocity, a key variable for sediment transport.

Tidal sand ridges can be classified, according to their present-day morphodynamic activity, as active (sand transport everywhere), quasi-active (sand transport on parts of the ridges) or inactive (no sand transport) [De Swart and Yuan, 2019]. Belderson et al. [1986] showed that the now inactive ridges in the Celtic sea could have been formed during a period with a lower sea level. This leads to the belief that active ridges can be 'drowned' if the sea level rises faster than the ridges can grow. Yuan and De Swart [2017] looked into the effects of SLR on tidal sand ridges and found that the time scale for ridges to become inactive is inversely proportional to the rate of SLR. However, this study uses a strongly idealized model with an open domain, a constant mean depth and schematized formulations for waves and sand transport. Building on previous knowledge, this study will look into the effects of SLR on tidal sand ridges, specifically those located along the Belgian coast, in a more realistic setting than any previous studies.

The knowledge gaps mentioned before lead to the formulation of the following research questions:

1. What is the impact of SLR on the characteristics of the tidal wave (amplitude/phase of water level and tidal current, for different constituents) on the shelf, as well as for the characteristics of wind waves (significant wave height, wave period, wave direction and wave orbital velocity near the bed).

2. What is the impact of solely SLR (present-day conditions of waves and tides) on the evolution of tidal sand ridges and how does the rate of SLR affect this?

3. As in 2, but also accounting for changes in the characteristics of the tidal and wind waves.

To answer these questions, the state-of-the-art coupled numerical morphodynamic model Delft3D-SWAN will be used, which solves for currents, waves, sand transport and bed level changes. This model will be discussed in section 2, together with the different model domains, the design of experiments and some background information on sand transport. The results are shown in section 3 and discussed in section 4. Section 5 contains a summary and the conclusions.

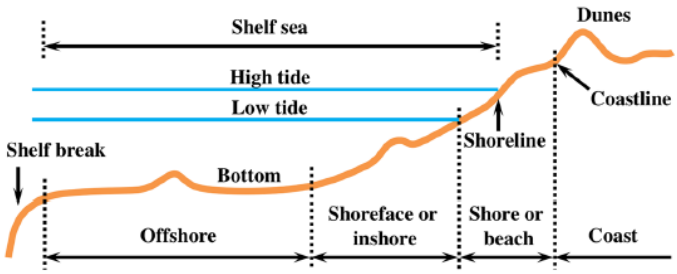

Figure 1: Schematic morphology of the continental shelf [De Swart and Yuan, 2019].

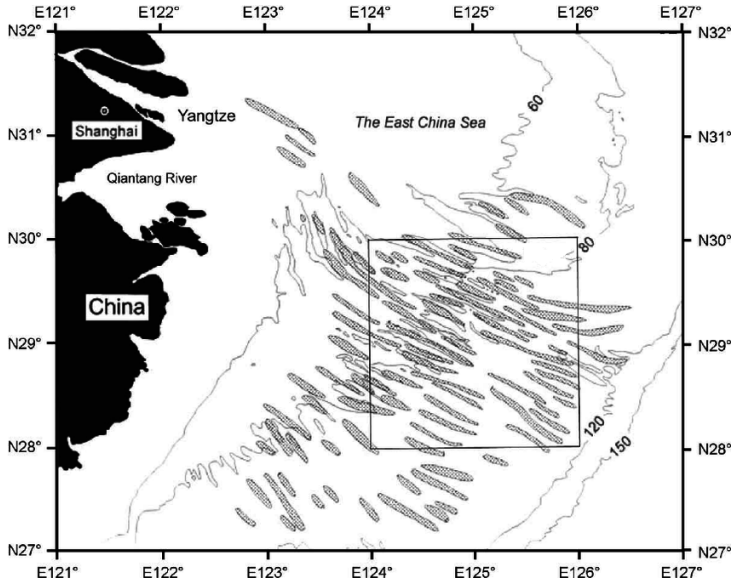

Figure 2: Tidal sand ridges in the East Chinese Sea [Liu et al., 2003].

2 Material and Methods

In this thesis several models will be used to simulate the tides, waves and morphodynamics in the three areas of interest. The model domains range from small to medium to large-scale. The small-scale domain represents the area of interest, which is part of the Belgian shelf. The model that governs the hydro- and morphodynamics on that domain will from now on be called the Belgian Shelf Model. The medium-scale domain represents the southern North Sea. On this domain only hydrodynamics is considered and the model is called the ZUNO model (ZUiderlijke NOordzee) [Roelvink et al., 2001]. The large-scale domain comprises the entire North Sea shelf area. The hydrodynamic model for that domain is called DCSM (Dutch Continental Shelf Model) [Verboom et al., 1992]. This chapter will discuss each of these models separately and elaborate on the variables of interest and the equations solved. It will also explain how these models are combined into a so-called model train.

2.1 The models

Each of the models is based on the model system Delft3D. This is a system with integrated modules that, amongst others, allows for simulations of (wave-averaged) currents, short wave generation and propagation, sediment transport and morphological changes. A detailed explanation about the modules

is given in Lesser et al. [2004], but a short overview will be given here. Figure 3 is a visualisation of the different models and the Delft3D modules used in each model. Figure 4 shows the domains of each of these models and how they are nested.

Model train	Delft3D modules			
	FLOW	SWAN	MOR	SED
BELGIAN SHELF MODEL	X	X	X	X
ZUNO+	X	X		
DCSM	X	X		

Figure 3: Different models versus Delft3D modules.

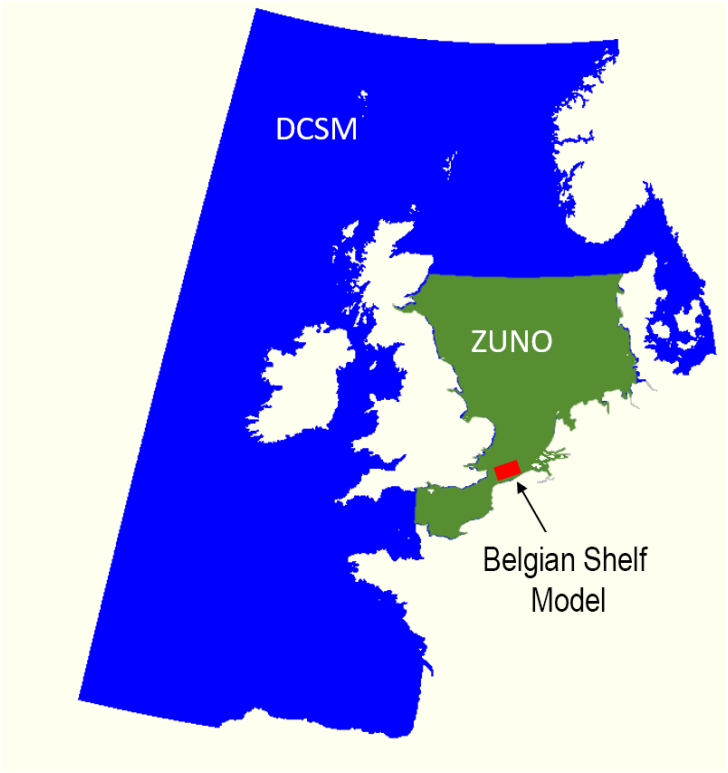

Figure 4: The three different model grids used in this study. The Belgian Shelf Model, the ZUiderlijke NOordzee model and the Dutch Continental Shelf Model.

2.1.1 Belgian Shelf Model

This model has the smallest domain and is used to study the local changes in morphodynamics. These changes are affected by changes in the tides and waves, which are therefore also modelled. Figure 5 shows the two different grids, one used for the larger computational domain for wave modelling (grey and blue) and on for the smaller physical domain, where tides and morphodynamics are modelled (blue). The physical domain represents the region of the Belgian coast seen in Figure 6. This domain is smaller than the computational domain to exclude boundary effects and to prevent wave shadow effects from affecting the results.

The model needs accurate boundary conditions for both waves and tides. For tides, the water level (ζ) is imposed on the west boundary, while the north and south boundary have Neumann boundary conditions ($\frac{\partial \zeta}{\partial y}$). On the eastern boundary, it is assumed that there is no cross-shore transport of fluid between the shelf and the nearshore zone, so the u-component of the velocity vanishes [Nnafie et al., 2020] and [Roelvink and Walstra, 2004]. As for the waves, a wave spectrum (including significant wave height, peak wave period and wave direction) is imposed on the north, south and west boundary. The specific values for tide and waves at these boundary are generated by the larger-scale models described in section 2.1.2.

The flow chart in Figure 7 shows an overview of the variables computed, the module used for the computation, and how the variables are connected. To calculate the morphodynamic changes, first the tides and waves need to be computed.

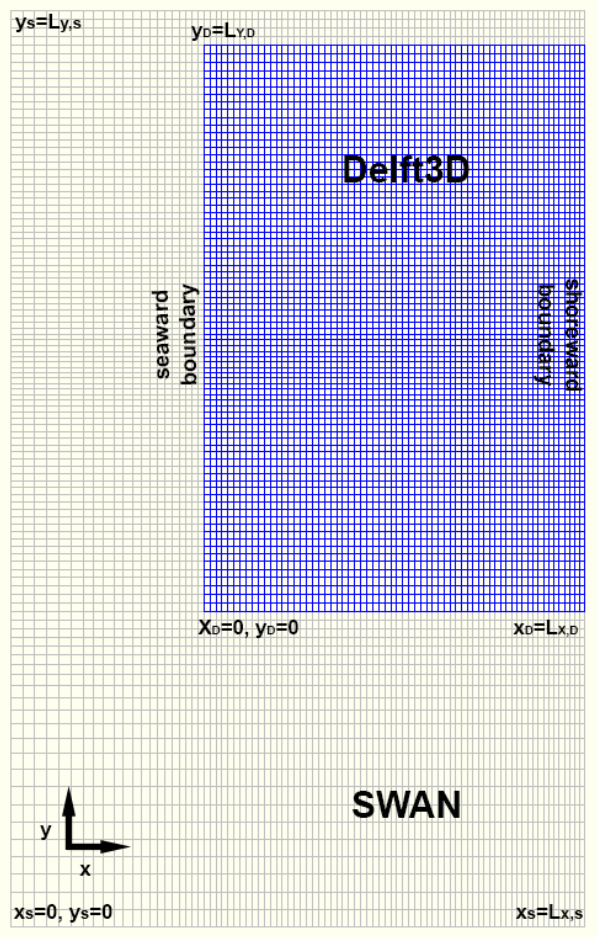

Figure 5: Delft3D-Flow and SWAN grid for the Belgian Shelf Model.

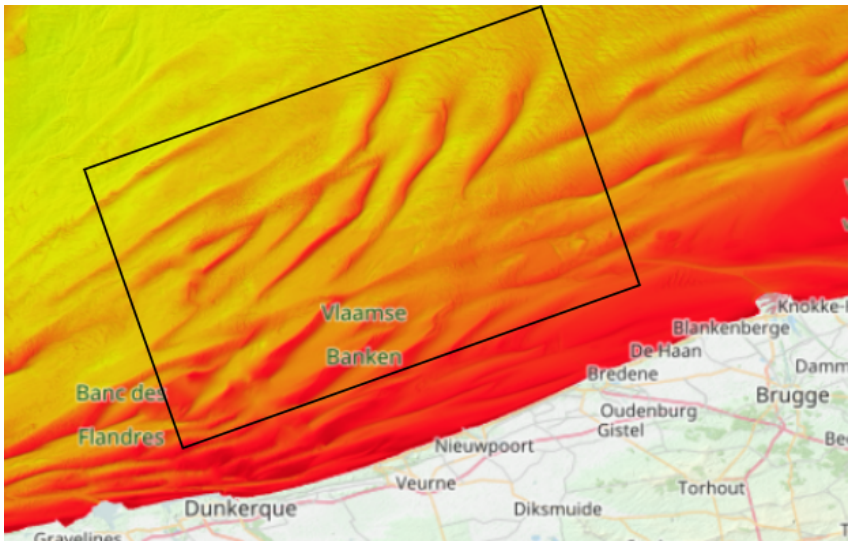

Figure 6: Location of the Belgian Shelf Model. Bathymetry retrieved from the EMODnet Bathymetry website.

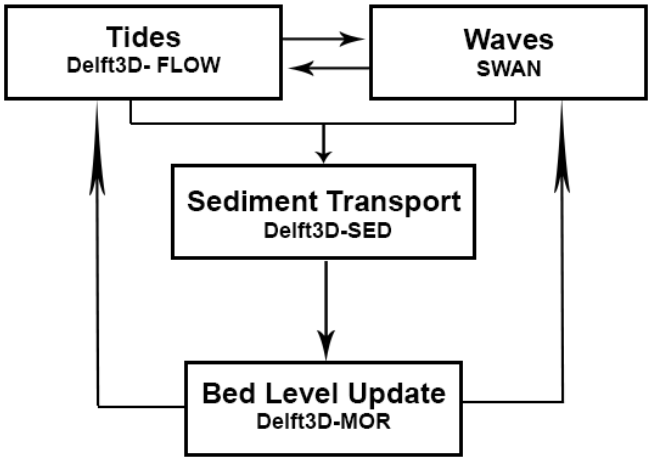

Figure 7: Flow Chart on coupling between the different Delft3D modules

The Delft3D module that calculates the hydrodynamic flow is called Delft3D-FLOW, which solves the three-dimensional non-linear shallow water equations. In this study, only the depth-averaged equations are used, which read:

$$\frac{\partial \zeta}{\partial t} + \frac{\partial (hu)}{\partial x} + \frac{\partial (hv)}{\partial y} = 0, \tag{1}$$

$$\frac{\partial u}{\partial t} + u\frac{\partial u}{\partial x} + v\frac{\partial u}{\partial y} - fv = -g\frac{\partial \zeta}{\partial x} - \frac{\tau_{bx}}{h} + \frac{1}{h}(\frac{\partial}{\partial x}(\nu_e h\frac{\partial u}{\partial x}) + \frac{\partial}{\partial y}(\nu_e h\frac{\partial u}{\partial y})) + \frac{1}{\rho h}F_x, \tag{2}$$

$$\frac{\partial v}{\partial t} + u\frac{\partial v}{\partial x} + v\frac{\partial v}{\partial y} + fu = -g\frac{\partial \zeta}{\partial y} - \frac{\tau_{by}}{h} + \frac{1}{h}(\frac{\partial}{\partial x}(\nu_e h\frac{\partial v}{\partial x}) + \frac{\partial}{\partial y}(\nu_e h\frac{\partial v}{\partial y})) + \frac{1}{\rho h}F_y. \tag{3}$$

Here, u and v are the depth-averaged velocities in the x and y direction respectively, ζ the sea surface elevation with respect to the undisturbed water level, h the water depth, f the Coriolis parameter, g the gravitational acceleration, τ_{bx} and τ_{by} the wave averaged bed-shear stress resulting from the joint action of waves and currents respectively in the x and y direction, ν_e the horizontal eddy viscosity and F_x and F_y the components of the wave-induced force by waves, determined by the divergence of the wave radiation stress tensor $\mathbf{S}$,

$$F_x = -[\frac{\partial \mathbf{S}_{xx}}{\partial x} + \frac{\partial \mathbf{S}_{xy}}{\partial y}]$$
$$F_y = -[\frac{\partial \mathbf{S}_{yx}}{\partial x} + \frac{\partial \mathbf{S}_{yy}}{\partial y}]$$

Here, $\mathbf{S}_{ij}$ are the radiation stresses which transfer j-momentum in the ith direction. These components depend on wave properties, like wave height, wavenumber and wave direction [Dingemans et al., 1987]. The components of this tensor are calculated in the Delft3D-WAVE module. The Delft3D-WAVE module used is the SWAN (Simulating WAves Nearshore) model. This is a third-generation spectral wave model that represents all physical processes explicitly [Booij et al., 1997]. When both waves and currents are present, the conserved wave quality is wave action (N), which is equal to the energy density (E) divided by the relative frequency (σ). Energy density is proportional to the square of the wave height and the wave amplitude is proportional to the wave period. This model solves the spectral wave action balance:

$$\frac{\partial N}{\partial t} + \frac{\partial c_{g,x} N}{\partial x} + \frac{\partial c_{g,y} N}{\partial y} + \frac{\partial c_\theta N}{\partial \theta} + \frac{\partial c_\sigma N}{\partial \sigma} = \frac{S}{\sigma}. \tag{4}$$

Here, N is the spectral wave action density, c_g the group velocity, θ the wave direction, σ the relative frequency and S the source and sink term. The first term on the left hand side represents the local rate of change of spectral action density (N), the second and third term represent the propagation of action density in the physical space with propagation velocities $c_{g,x}$ and $c_{g,y}$. The fourth term represents

the depth- and current-induced refraction, with propagation velocity in the wave direction space c_θ and the fifth term represents the frequency shift due to variations in currents, with propagation velocity in the frequency space c_σ. The righ- hand side represents all source and sink terms of wave energy. Including generation due by wind, dissipation by whitecapping, bottom friction, depth-induced breaking and redistribution of energy in the wavenumber space by non-linear wave interactions.

Sediment transport is calculated using the Delft3D-SED module. The total transport is calculated by the sum of the bed load transport and the suspended load transport [Dissanayake, 2009]. The physics of these different modes of transport are discussed in section 2.2.2. The bed load transport is by calculated using the following equation by Van Rijn et al. [1993]:

$$|S_b| = \eta 0.006 \rho_s w_s d_{50} M^{0.5} M_e^{0.7}. \tag{5}$$

Here, η is the relative availability of sediment at the bottom, ρ_s is the density of the sediment particles, w_s is the sediment fall velocity, d_{50} is the median sediment diameter, M is the sediment mobility number due to waves and currents and M_e is the excess sediment mobility:

$$M = \frac{v^2 + U_w^2}{(s-1)gd50}, \tag{6}$$

$$M_e = \frac{[\sqrt{v^2 + U_w^2} - v_{cr}]^2}{(s-1)gd_{50}}, \tag{7}$$

In these expressions, U_w is the near-bed peak orbital wave velocity (computed by SWAN), s the density of sediment divided by the density of water and v_{cr} the critical depth-averaged velocity, consisting of a part due to currents and a part due to waves. The critical velocity will also be discussed in section 2.2.2.

The suspended load transport is computed with the following integration [Van Rijn, 1984]:

$$|S_{sus}| = \int_h^0 cudz \tag{8}$$

c is the depth averaged sediment concentration, which will be approximated by the depth-integrated advection–diffusion equation:

$$\frac{\partial hc}{\partial t} + u\frac{\partial hc}{\partial x} + v\frac{\partial hc}{\partial y} - D_H\frac{\partial^2 hc}{\partial x^2} - D_H\frac{\partial^2 hc}{\partial y^2} = \frac{w_s(c_{eq} - c)}{T_s}. \tag{9}$$

Here, D_H is the horizontal eddy diffusion coefficient, c_{eq} is the depth-averaged equilibrium concentration, w_s the settling velocity and Ts is an adaptation time scale ($\propto$ water depth over settling velocity) [Dissanayake, 2009]. The bed level is dynamically updated in the Delft3D-MOR module, using the following formula:

$$\frac{\partial z_b}{\partial t} = -\frac{1}{1-p}[\frac{\partial S_{b,x}}{\partial x} + \frac{\partial S_{b,y}}{\partial y} + \frac{w_s(c_{eq} - c)}{T_s}]. \tag{10}$$

Where z_b is the bed level and p the porosity of the bed.

The hydrodynamic processes act on a shorter time scale than the morphodynamic processes. The difference can be several orders of magnitude. To solve this problem the morphological acceleration factor is introduced (f_{MOR}). This factor allows for accelerated bed level changes and couples the hydrodynamic and morphodynamic time scales.

$$\Delta t_{morphology} = f_{MOR} * \Delta t_{hydrodynamics}. \tag{11}$$

2.1.2 ZUNO+ and DCSM models

The ZUNO Model is an existing model of the southern North Sea, which computes tides [Roelvink and Walstra, 2004]. In this thesis the SWAN module was added, so that waves are also accounted for. Therefore, it will from now on be called the ZUNO+ Model. The output of ZUNO+ is used to specify the forcing at the boundaries of the Belgian Shelf Model. The model grid covers the area between the English Channel up until the north of Denmark (see Figure 4). The existing DCSM Model, which covers the entire North Sea shelf area, is able to compute tides, but can also generate wind waves.

The ZUNO+ boundary conditions are derived from the DCSM model in two ways. When modelling waves, the ZUNO+ model is nested into the DCSM model, which links them directly. When modelling tides, the DCSM model is simulated first and the time series at the location of the ZUNO+ boundaries

are extracted. These time series are put into the ZUNO+ model as boundary conditions. By doing this, the computational time is reduced. In case of the DCSM model, there is no larger-scale model to provide boundary conditions, therefore, another approach was used. The astronomical tide is used, assuming the water depth at the boundaries is large enough for overtides to be absent. Regarding the wave conditions, it was found that on domains that have sizes like those of ZUNO+ and DCSM, the SWAN model cannot accurately solve for swell and wind waves at the same time. Therefore, the choice was made to generate wind waves in the DCSM model (and consequently also in the nested ZUNO+ model). Using this approach, only the wind speed and wind direction are needed at the boundaries of the DCSM model. This data comes from two buoys in the North Sea (see red circles in Figure 8). From this, several scenarios were constructed. The wind data was split up into eight different wind direction bins (north $[337.5^o - 22.5^o]$, north-east $[22.5^o - 67.5^o]$, east $[67.5^o - 112.5^o]$, etc.) and in two wind speed conditions ($< 10.5\,\mathrm{m/s}$ or $\geq 10.5\,\mathrm{m/s}$), so 16 different wind scenarios in total. Each of these scenarios had a corresponding probability, based on the number of occurrences in the dataset. With each of these wind scenarios a model run was done, which calculates the waves for the specific conditions. Using the corresponding probabilities, average wave conditions were constructed. In all model runs the wind climate was kept constant, meaning neither the wind directions and speeds, nor the probabilities were changed.

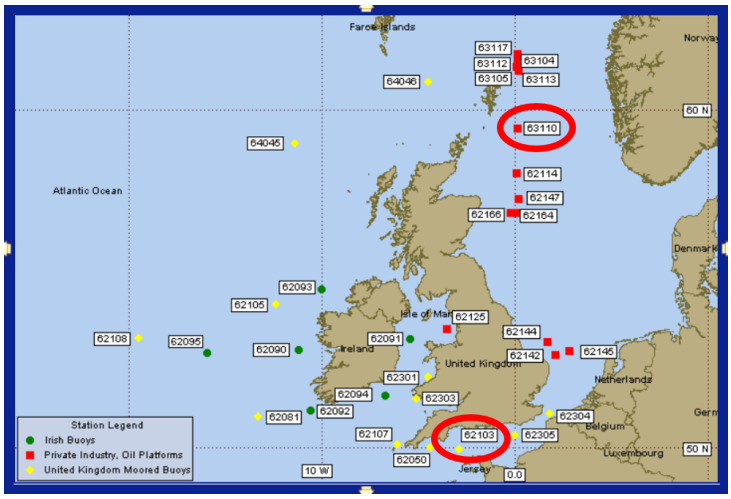

Figure 8: Location of buoys used for wave analysis.

2.1.3 Numerical aspects and choices of model parameters

The Delft3D and SWAN solve the equations on rectilinear staggered grids (Figure 5). The physical domain in the Belgian shelf model has a cross-shore width $L_{xD} = 50\,\mathrm{km}$, a alongshore length $L_{yD} = 75\,\mathrm{km}$ and a grid size of about 800 m. Here, the tide and morphodynamics is modelled by Delft3D. The larger computational grid, where the waves are modelled by SWAN, has a cross-shore width $L_{xS} = 75\,\mathrm{km}$, an alongshore length $L_{yS} = 120\,\mathrm{km}$ and a grid size ranging from 800 m nearshore to $\approx 2000\,\mathrm{m}$ offshore. A linear depth profile is chosen, with a depth $h_{sea} = 38.5\,\mathrm{m}$ at the seaward boundary and $h_{shore} = 5\,\mathrm{m}$ at the shore boundary. The tidal and wave forcing at the boundaries was extracted from the ZUNO+ results for present-day conditions. This lead to a M_2 tidal wave traveling from south to north, with a tidal period of $T = 12.41\,\mathrm{h}$, an amplitude of $\zeta = 1.55$ and phase of $\phi = 235.4^o$ at the southern point of the western boundary and an amplitude of $\zeta = 0.92\,\mathrm{m}$ and a phase of 14.6^o at the northern point of the western boundary. Wave spectra are imposed on the south, west and north boundary of the SWAN model domain. With significant wave height $H_{sig} = 1.67, 1.74, 1.73\,\mathrm{m}$, respectively, peak wave period $T_p = 5.76, 7.79, 7.84\,\mathrm{s}$, respectively and wave direction $\theta = 270^o$ at all boundaries. These boundary conditions were adjusted when SLR effects came into play. This was done by using a WaveCon file [Deltares, 2019b] when changing the wave boundaries and a time series file [Deltares, 2019a] when changing the tidal boundaries.

The Delft3D-FLOW and SWAN modules run separately and are coupled through communication files. The WAVE module runs and stores the results on wave height, wave period, wave direction, etc. The FLOW module will use these results in the next calculations. The new velocity fields will be stored and in turn used in the new WAVE calculations [Lesser et al., 2004]. The communication time between

the modules is 60 minutes. As the morphological timescale is much longer than the hydrodynamic time scale, a morphological acceleration factor $f_{MOR} = 200$ was used. There is a limit to this acceleration factor, but as long as the bed level changes do not exceed 5% of the water depth this methodology is justified according to Roelvink [2006]. An overview of all model parameters in the Belgian Shelf Model is presented in Table 1.

Table 1: Default model parameters Belgian Shelf Model. Adjusted from Wolf [2019] and Nnafie et al. [2020].

Parameter	Value	Description
Physical domain		
$L_{x,D}$	50 km	Width of domain
$L_{y,D}$	75 km	Length of domain
h_{sea}	38.5 m	Depth at seaward side
h_{shore}	5.0m	Depth at landward side
Flow		
f	$1.43\text{x}10^{-4}\text{s}^{-1}$	Coriolis parameter
ν_e	1 m^2s^{-1}	Eddy viscosity
ζ_S, ζ_N	1.55m, 0.92m	Amplitude M_2 at South and North point of western boundary
ϕ_S, ϕ_N	$352.4^o, 14.6^o$	Phase M_2 at South and North point of western boundary
ω	$1.405\text{x}10^{-4}$ s^{-1}	Angular frequency M_2 tide
SWAN		
f_s	[0.05 2] Hz	Range of frequency
bins	40	Number of frequency bins
B_f	0.035 m^2s^{-3}	Bottom friction, JONSWAP
H_{sig}	1.74 m	Significant wave height at western boundary
T_p	5.79 s	Peak wave period at western boundary
θ	270^o	Wave direction at western bounary
Sediment		
η	1.66	Relative availability of sediment
d_{50}	200 μm	Grain size diameter
ρ_s	2650 kgm^{-3}	Sediment density
ρ	1024 kgm^{-3}	Water density
D_H	0.2 m^2s^{-1}	Horizontal eddy diffusivity
p	0.4	Porosity of bed
Numerics		
Δt	60 s	Time step
T_{com}	60 min	Communication time Delft3D-Flow and SWAN
f_{MOR}	200	Morphological acceleration factor

The DCSM grid covers the area from -12^o to $+9^o$E and 48^o to 64^oN and has a grid resolution of $1/20^o$ x $1/30^o$ ($\approx$ 3.6 km x 3.6 km). The ZUNO grid covers the area from approximately -3^o to $+9^o$E and from 49^o to 57^oN. It is a curvilinear, staggered grid with resolutions ranging from 200m (nearshore) to 2 km [Gautier and Caires, 2015]. In this grid the water level points and depth-points are co-located in the cell centres and the u- and v- velocity points are located in the middle of the cell walls [Roelvink, 2006].

The ZUNO model was run over the period of 2-1-2007 to 9-1-2007, this time frame falls in between the spring and neap tide. This was done in order to get a impression on the average tide in the North Sea, but saves on computational time, by only modelling a couple of tidal cycles (instead of e.g. a year, or several years).

2.2 Experiments

To answer the research questions, several experiments were conducted. First the impact of SLR on tides was investigated with the ZUNO model. Similar to Pickering et al. [2012], tides were modeled for a default case without SLR, for cases between 0 and 2 meters SLR and for a case with 10 meters SLR. The

phase, amplitude and tidal currents of different tidal constituents are analysed and compared for these different cases.

The impact of SLR on waves was investigated with the ZUNO+ model, by creating the mean wave conditions from the 16 scenarios discussed in section 2.1.2. Similar to the tidal experiments, for a default case, for cases between 0 and 2 meter SLR and for a case with 10 meter SLR. The significant wave height, the peak period, the wave direction and the orbital velocity at the bed are analysed and compared.

The gathered information on tides and waves were used as a forcing in the morphodynamic model. First, the present-day tidal and wave conditions were used to force the model, to see how the tidal sand ridges would evolve without any SLR. Next, the forcing was kept the same, but the water depth increased. This time, not in steps, like in the tide and waves experiments, but by gradually increasing the water depth, giving the tidal ridges time to adjust to a new equilibrium. The rates of SLR are those of present-day SLR and of projections done by the IPCC [Church et al., 2013] (see Figure A1). The same experiments were done, but including the previously found changes in wave forcing and later also including the changes in tidal forcing, to see how this would affect the morphodynamic features. An overview of these experiments and in which model domain they were executed can be found in Table 2.

Table 2: List of model runs and in which model domain it was executed. (BSM=Belgian Shelf Model)

Run name	Description	Model
PresentTides	Present-day tidal conditions	ZUNO
Tides2mSLR	Tidal conditions with 2 m SLR	ZUNO
Tides10mSLR	Tidal conditions with 10 m SLR	ZUNO
PresentWaves	Present-day wave conditions	ZUNO
Waves2mSLR	Wave conditions with 2 m SLR	ZUNO
Waves10mSLR	Wave conditions with 10 m SLR	ZUNO
SpinUp	Spin-up run for TSR	BSM
SLRPresentDay	Morphological run with present-day conditions for waves and tides and a SLR ranging form 2-11 mm/yr	BSM
SLRWaves	Morphological run with present-day conditions for tides, future conditions for waves and a SLR ranging form 2-11 mm/yr	BSM
SLRWavesTides	Morphological run with future conditions for waves and tides and a SLR ranging form 2-11 mm/yr	BSM

2.2.1 Analysis of model results

The model results were analysed in several ways. First, a harmonic analysis of the water level was done. The water level signal is divided into several tidal constituents, such as the M_0, M_2 and M_4. The u-tide function was used for this. This function determines a constituent by confirming it is independent from other included constituents, by checking the significance relative to noise and to other constituents and by characterizing the reconstructed harmonic fits [Codiga, 2011]. This function also calculates the tidal current for each constituent.

Second, to determine the height of the ridges, the root-mean square ridge height is calculated (the integral of the square heights). From this, the growth rate was calculated, by dividing the change in h_{rms} over time. An indication of whether the tidal sand ridges can keep pace with the rising sea level is found when dividing the growth rate over the rate of SLR.

Finally, to determine the location of the sediment in the domain a sand volume balance of the shelf domain is carried out. The relative changes of the total volumes of all the crests and troughs are analysed, as well as the relative changes of the sand volume that is lost or gained through the model boundaries. These volumes are computed using the formulations by Nnafie et al. [2020]:

$$V_C(t) = \int\int_A h\Theta(h)dxdy, \tag{12}$$

$$V_T(t) = \int\int_A h(1-\Theta(h))dxdy, \tag{13}$$

$$V_{BND} = V_C(t) - V_T(t). \tag{14}$$

Here, $\Theta(h)$ is a Heaviside step function with $\Theta(h) = 0$ for $h \leq 0$ and $\Theta(h) = 1$ for $h > 0$ and A is the surface area of the shelf. To calculate the sediment lost or gained over each boundary separately, the residual transport was integrated over each boundary.

2.2.2 Background information on sand transport

The effects of currents and waves primarily take place through the friction they exert on the bed, this is expressed in terms of the bed shear-stress. The magnitude of the bed shear-stress depends both on the speed of the flow and the roughness of the bed. The total bed shear-stress is made up of skin friction (produced by the sediment grains), form drag (produced by the pressure field associated with flow over bed features) and sediment transport (caused by momentum transfer to mobilise grains) [Soulsby, 1998]. For sediment particles to start moving a critical bed shear stress has to be reached. This can also be expressed in terms of velocity. The critical velocity is the velocity at which grains of sediment begin to move [Soulsby, 1998]. The magnitude of both of these parameters depends mainly on grain-size [Andersen et al., 2007]. On a sloping bed, gravity provides a force on the grains which may increase or decrease the critical shear-stress (and velocity), depending on the direction of the flow and the slope. There are two way sediment can be transported through the domain, which are sketched in Figure 9, by bed load transport (through sliding, rolling and saltating) or by suspended load transport.

When the wave orbital motion near the bed is higher than the critical velocity, sediment will be transported in the direction of wave propagation. Tidal currents can also transport sediment. However, with a pure M_2 tide the sediment transport over a tidal cycle averages to zero. When adding a single overtide M_4, the tidal wave becomes asymmetric and the influence by the ebb and flood phase on sediment transport are no longer the same. The phase angle between the two constituents determines the direction of the transport [Van de Kreeke and Robaczewska, 1993].

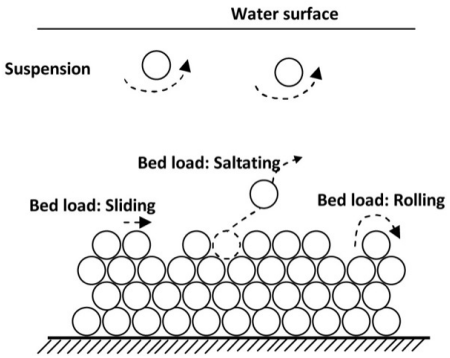

Figure 9: A sketch of bed load and suspended load transport by Gao [2010].

3 Results

3.1 Effects of sea level rise on tides

3.1.1 Present-day conditions

Figure 10a shows the results of the ZUNO+ model for the sea surface elevation related to the M_2 tide under present-day conditions in the southern North Sea. The colors represent the tidal amplitude and the black lines the tidal phase. Figure 10b shows the measured M_2 tide in the North Sea [Reynaud and Dalrymple, 2012]. The black lines with the bold numbers are the lines of equal tidal amplitude and the black lines with the regular numbers are the phase lines. The locations where the phase lines meet are amphidromic points. The amplitude in the amphidromic points is (close to) zero. In these figures, three amphidromic points are present, to the north of the Netherlands, in between the Dutch and the British coast (the Southern Bight) and in the south of England (on land). The locations are approximately the same for the modelled and the observed tide, as are the phase lines connected to them. Along the eastern British coast the amplitude reaches up to 2 m and it is even higher in the English Channel, while along the Dutch coast it reaches 1 m. This corresponds to the observed M_2 tide, as well. The tidal wave travels counter-clockwise around the amphidromic points, which means it travels from south to north along the Belgian coast. More detailed figures of the M_2 tide for the Belgian coastal area are given in

the Appendix Figure A2a. This figure shows the tidal wave with an amplitude of ≈ 1.5 m travelling from southwest to northeast along the Belgian coast.

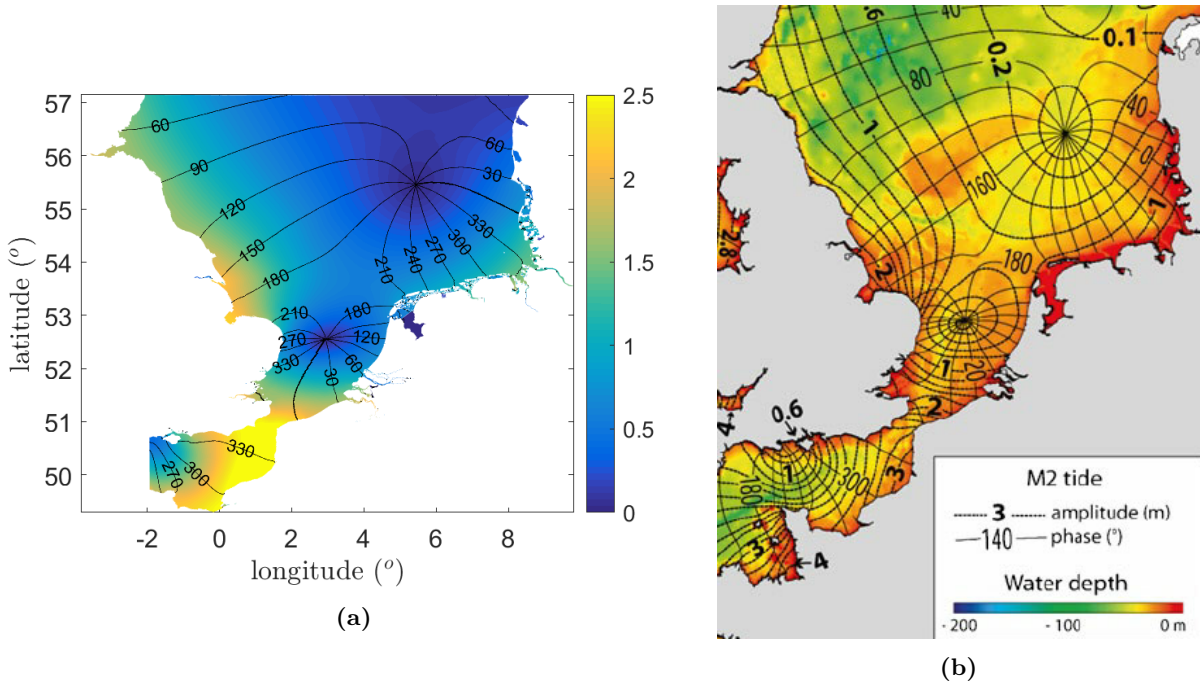

(a) (b)

Figure 10: a M_2 sea surface elevation computed by the ZUNO+ model for present-day conditions in the Southern North Sea. Black lines represent tidal phase in degrees, the colors represent tidal amplitude in m. Figure **b** shows a map of the measured M_2 amphidromic systems in the North Sea. [Reynaud and Dalrymple, 2012]

The M_4 tidal constituent is created due to non-linear interactions in shallow water [Gerkema, 2019, and references herein]. The addition of the M_4 constituent to the M_2 tide results in an asymmetric tidal wave. Figure 11a shows the M_4 tide in the ZUNO+ model, with the amplitude in meters as the background color and the phase in degrees as the black lines. Similar to the M_2 tide, the tidal constituent travels counter-clockwise around amphidromic points. Figure A2b shows a zoom-in for the Belgian shelf. The M_4 constituent travels from southwest to northeast with an amplitude of 0.2 m.

The modelled residual sea surface height in the North Sea is shown in Figure 11b. The same is shown in Figure 11c, but computed by Prandle [1978]. Both figures show the same pattern; high amplitudes along the Dutch coast and low amplitudes in the English Channel. The amplitudes are in the same order of magnitude, but do not match exactly, which is likely due to the higher resolution used in the ZUNO+ model. This pattern will lead to a residual current flowing from high to low amplitudes. So from north to south, along the Dutch, Belgian and French coast. This can also be seen in the zoom-in figure in the Appendix (Figure A2c).

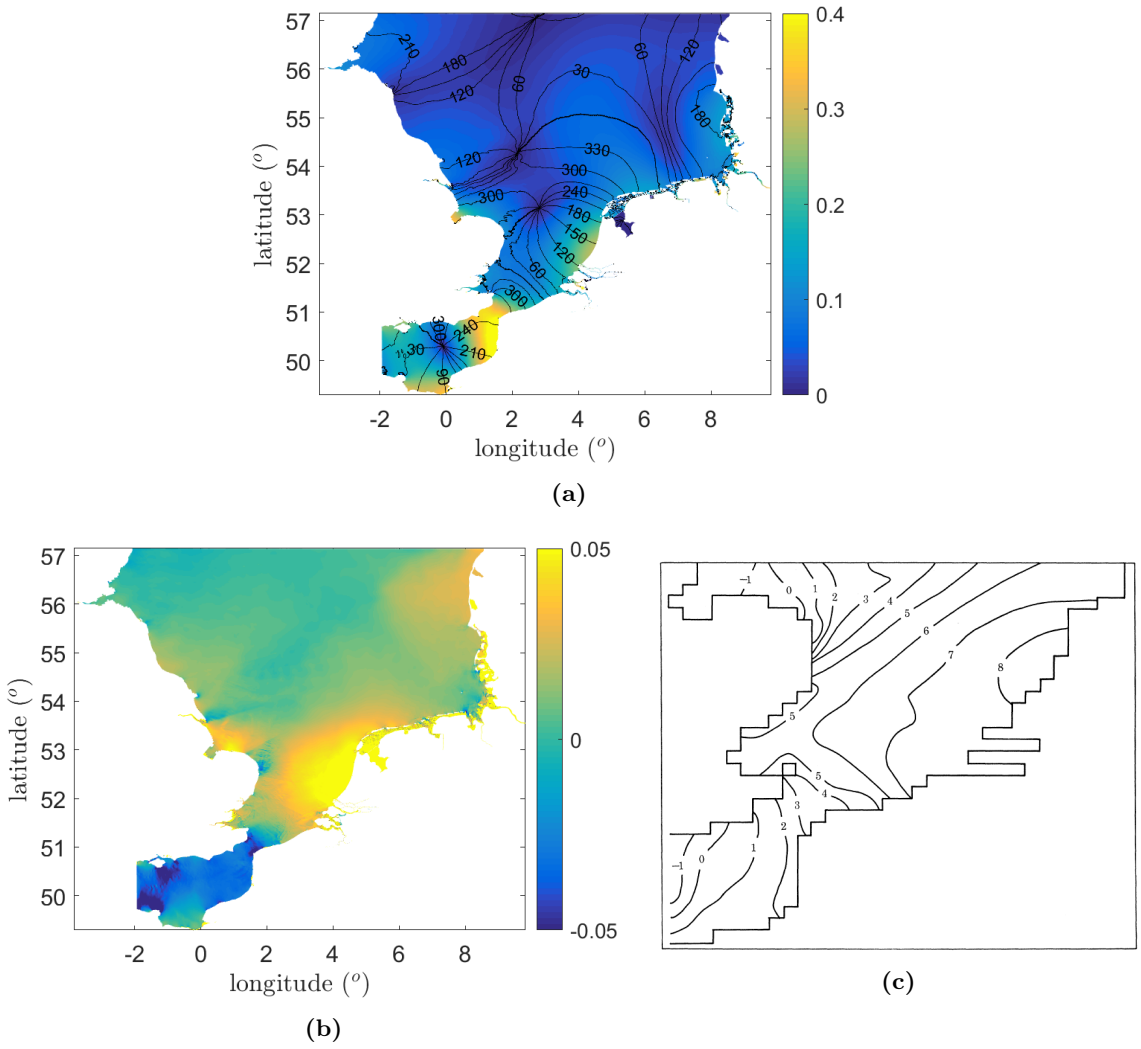

Figure 11: **a** M_4 tidal constituent of sea surface variation in the ZUNO+ model for present-day conditions. Colors represent the water level in m and the black lines represent the phase in degrees. **b** M_0 tidal constituent in the ZUNO+ model for present-day conditions. Colors represent the water level in m. **c** M_0 amplitude [cm] in the southern North Sea computed by Prandle [1978].

In Figure 12a the M_2 tidal ellipses computed by the ZUNO+ model is shown and Figure 12b shows the tidal current (major axis of the ellipse) and the phase. In the Northern North Sea the major axes are mostly orientated in a north-south direction. The tidal current velocities range from 0.6 ms^{-1} near the British coast to 0.1 ms^{-1} away from the coast. Both clockwise and counter-clockwise rotating currents are found here. Along the northern Dutch coast the major axes are orientated in a east-west direction. Here and in the Southern Bight, the currents magnitude is in the order of 0.25 ms^{-1}. Finally, in the English Channel, the current is almost rectilinear, with magnitudes up to 1.5 ms^{-1}. These results are very similar to the results found by Davies and Furnes [1980] (Figure 12c). The velocities and the orientations of the major axis in all locations of the North Sea match the results. However, the rotation of the ellipses is slightly different. Davies and Furnes [1980] find clockwise rotating ellipses in the Northern North Sea and counter-clockwise ellipses in the Southern Bight. Here, both of these areas show a combination of clockwise and counter-clockwise rotating ellipses. This could be explained by the fact that the model used in this study has a higher resolution compared to the model by Davies and Furnes [1980].

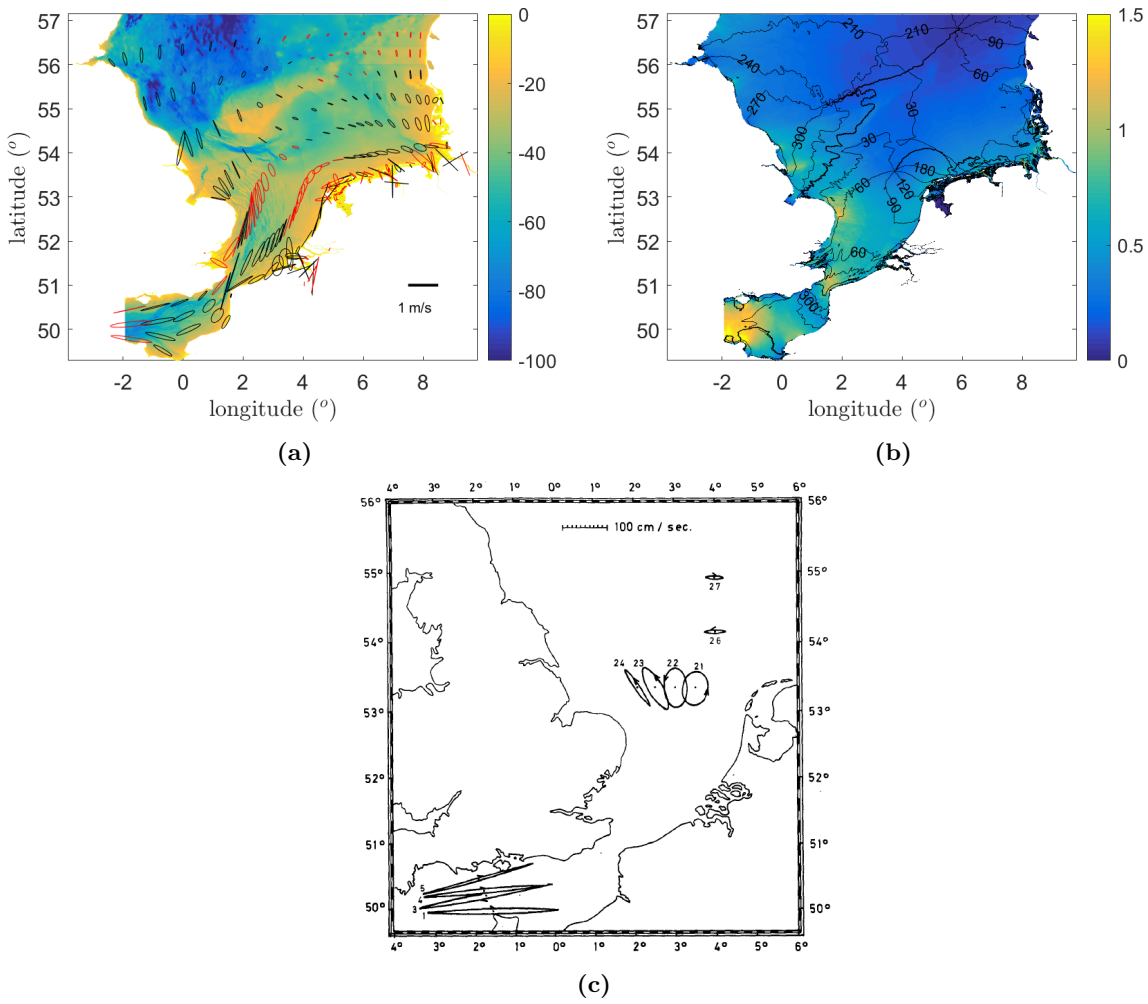

Figure 12: **a** Tidal ellipses of M_2 tidal current as calculated by the ZUNO+ model for present-day conditions. The background colors represent the bathymetry in m. The red ellipses indicate a clockwise rotation and the black ellipses a counterclockwise rotation. **b** The M_2 tidal current in m/s (colors) and the phase in degrees (black lines). **c** The M_2 tidal ellipses in the North Sea, modelled by Davies and Furnes [1980], based on current measurements.

3.1.2 Influence of sea level rise on tides

Based on the approach by Pickering et al. [2012], two SLR cases were examined. In both cases the water depth was increased at once, either by 2 m or 10 m. Figure 13 shows the model results, while Figure 14 shows the results obtained by Pickering, both figures subtract the default case from the SLR cases. In Figure 13 the black and magenta lines represent the phase of the default case and the SLR case, respectively. Remembering that the tidal wave travels in a counter-clockwise direction, in the SLR cases the tidal wave travels faster. In the case of 2 m SLR (Figure 13a), the amphidromic points shift only slightly and in a similar fashion as in Figure 14a. This leads to a similar pattern in the change in amplitude, which is shown as the background colors in all figures. However, for 10 m SLR, Figures 13b and 14b show very different results. The difference in the shift of the amphidromic point also leads to a difference in amplitude change. Nevertheless, the order of magnitude is the same between the two models. The difference between these models could, again, be due to the improved model resolution used in this study. The tidal amplitude increases along the Dutch and Belgian coast, while it decreases along the British coast. This is also seen in observations, showed in Figure 15. This figure shows the change in M_2 tidal amplitude most likely caused by SLR [Flanders Hydraulics Research, Antwerp]. There is a clear increase along the Dutch coast, while the amplitude along the British coast shows both an increase and a decrease, depending on the location.

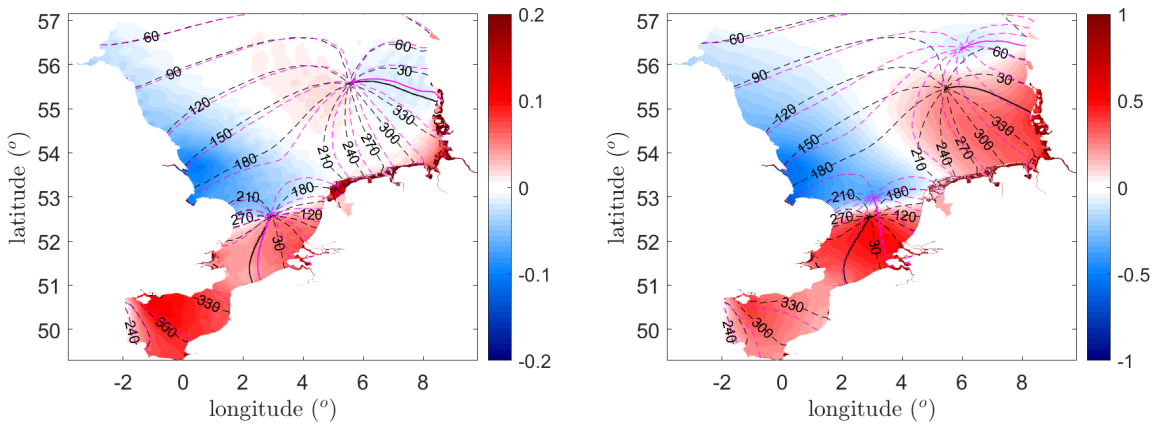

Figure 13: Different phase lines of the M_2 tide. The black lines represent the phase lines of the default case, the magenta lines represent the phase lines of the SLR case. The background colors show the changes in sea surface amplitude in meters between 2 m SLR (**a**) or 10 m SLR (**b**) and the default case in the ZUNO+ model.

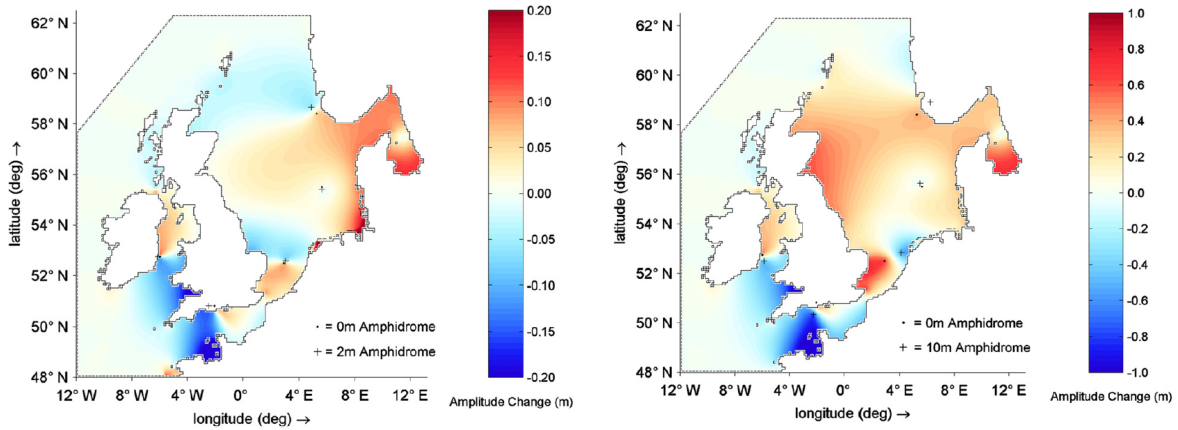

Figure 14: Plot of the change in M_2 sea surface amplitude and shift in amphidromic points with 2 m SLR (**a**) and 10m SLR (**b**) by Pickering et al. [2012].

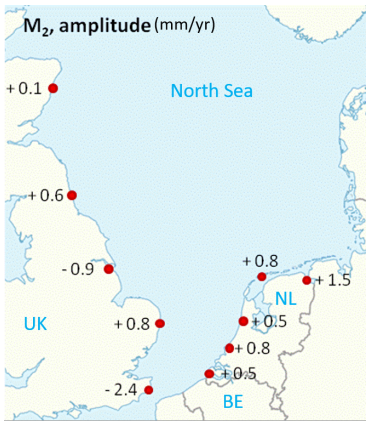

Figure 15: Observed changes in M_2 sea surface amplitude are most likely caused by SLR [Flanders Hydraulics Research, Antwerp].

The change in tidal current is shown in Figure 16, again for 2 m SLR (16a) and 10 m SLR (16b). Note the different scales on the colorbars. Along the Belgian, Dutch and Danish coast the tidal current increases, which will lead to an increase in sediment stirring. Along the British coast, the tidal current decreases, which also decreases the amount of sediment stirring.

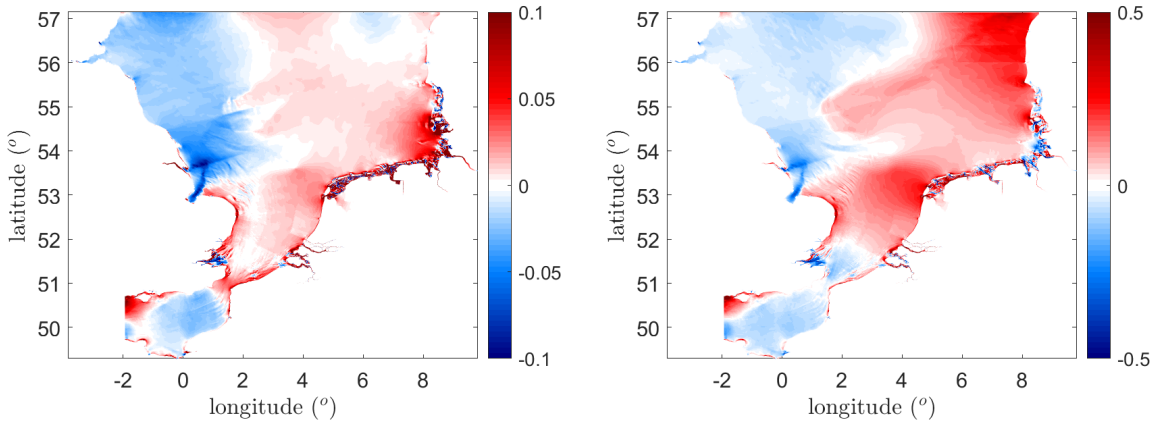

(a) **(b)**

Figure 16: Difference in amplitude of M_2 tidal current (or tidal ellipse major axis) in m/s between 2 m SLR (**a**) or 10 m SLR (**b**) and the default case in the ZUNO+ model.

To examine the local effects of SLR on tides on the Belgian shelf, several runs were done, each time with a slightly increasing water depth, between the range of 0 to 2 m SLR. The M_2 tidal amplitude, phase and velocity, as well as the M_4 and M_0 (residual) tidal velocity at the southern point of the Belgian Shelf Model are shown in Figure 17 (Location $x_D = 0, y_D = 0$ in Figure 5). The horizontal axis shows the amount of SLR in meters. The tidal amplitude and phase are used as boundary conditions in the morphodynamic runs that include the effect of SLR on tides. It seems that there is a almost linear increase in tidal amplitude, while there is a almost linear decrease in tidal phase. A decreasing tidal phase means that at this location the tidal wave will arrive sooner, indicating a faster travelling wave. The tidal velocity shows a different response to SLR. At first it increases with rising sea level, but a maximum is reached around 1 m SLR, after which the velocity decreases with a rising sea level. Note that the change in velocity is only in the order of mm/s. For the M_4 and M_0 constituents, the tidal velocity decreases with increasing SLR. This indicates less sediment stirring due to tidal currents with an increasing sea level.

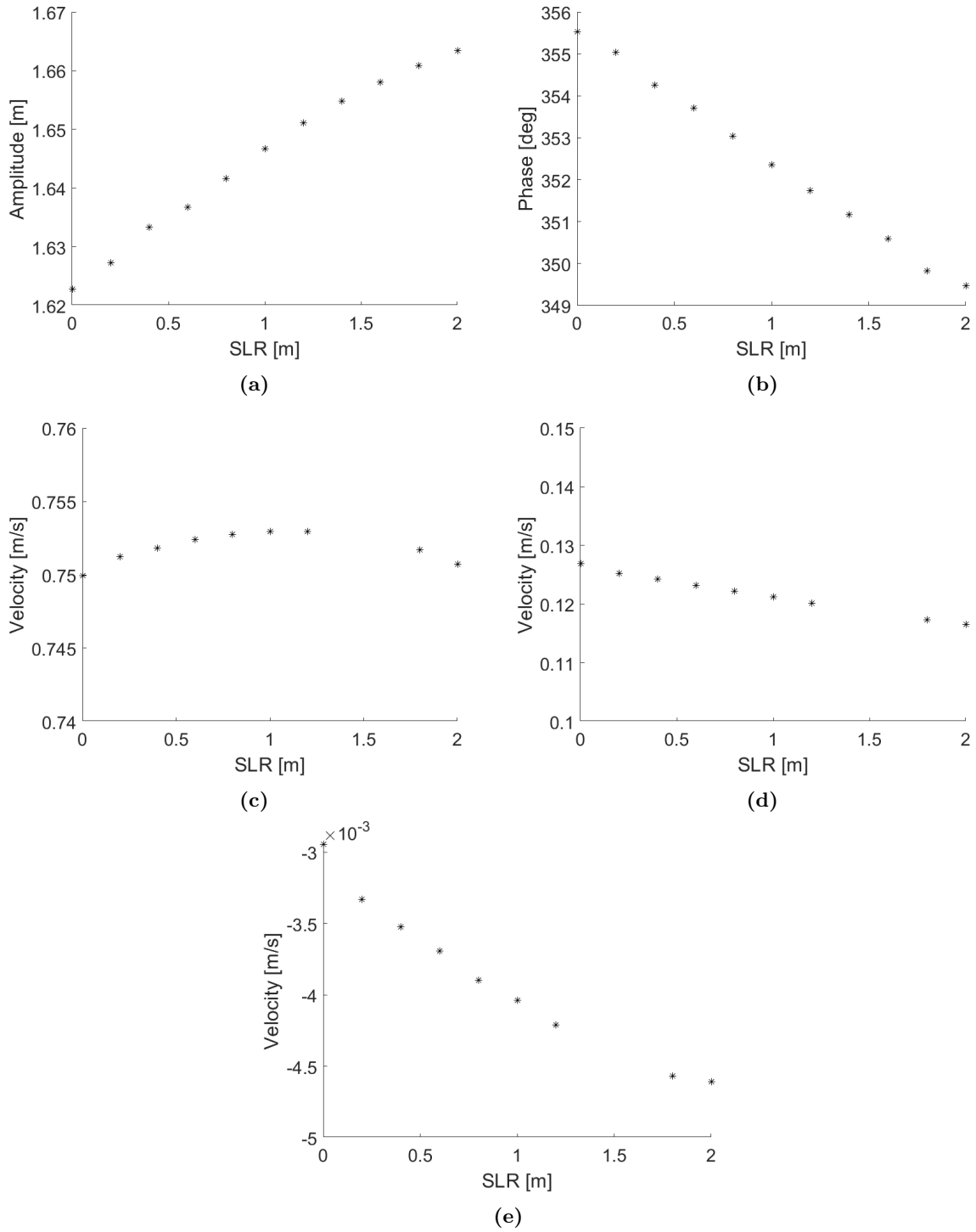

Figure 17: The M_2 tidal amplitude (**a**), phase (**b**) and velocity (**c**), the M_4 tidal velocity (**d**) and the M_0 tidal velocity (**e**) at the southern point on the western boundary of the Belgian Shelf Model versus sea level rise. The M_0 (residual) tidal velocity is negative, because it flows from north to south.

3.2 Effects of sea level rise on waves

3.2.1 Present-day conditions

Figure 18 shows the mean wave conditions in the southern North Sea, as calculated by the ZUNO+ model, for present-day conditions. Figure 18a shows the significant wave height [m] and the wave direction [^{o}], Figure 18b shows the peak wave period and Figure 18c shows the root-mean-square orbital velocity near the bottom [m/s]. These average wave conditions are constructed from runs with different wind

conditions and corresponding probabilities, discussed in section 2.1.2. To see if the average conditions are modelled accurately, the results are compared to the results found by Neill et al. [2009] (Figure 19). Neill finds slightly higher values for both the significant wave height and the peak wave period. This is likely due to the difference in wind forcing between the two models. In this study, the wind data is based solely on two buoys, whereas Neill uses ECMWF-ERA-Interim reanalysis data to force the model. In table 3 a comparison between the modelled and observed data for the significant wave height, peak period and wave direction is shown. Unfortunately, most locations do not have data on wave direction. Most of the time the model underestimates both the significant wave height and the peak period, probably due to the absence of swell waves. Zoom-ins on the Belgian shelf are shown in Appendix, Figures A3a and Figure A3b. They show a significant wave height of approximately 1.2 m, a direction of 170^o and a peak wave period of 5 s.

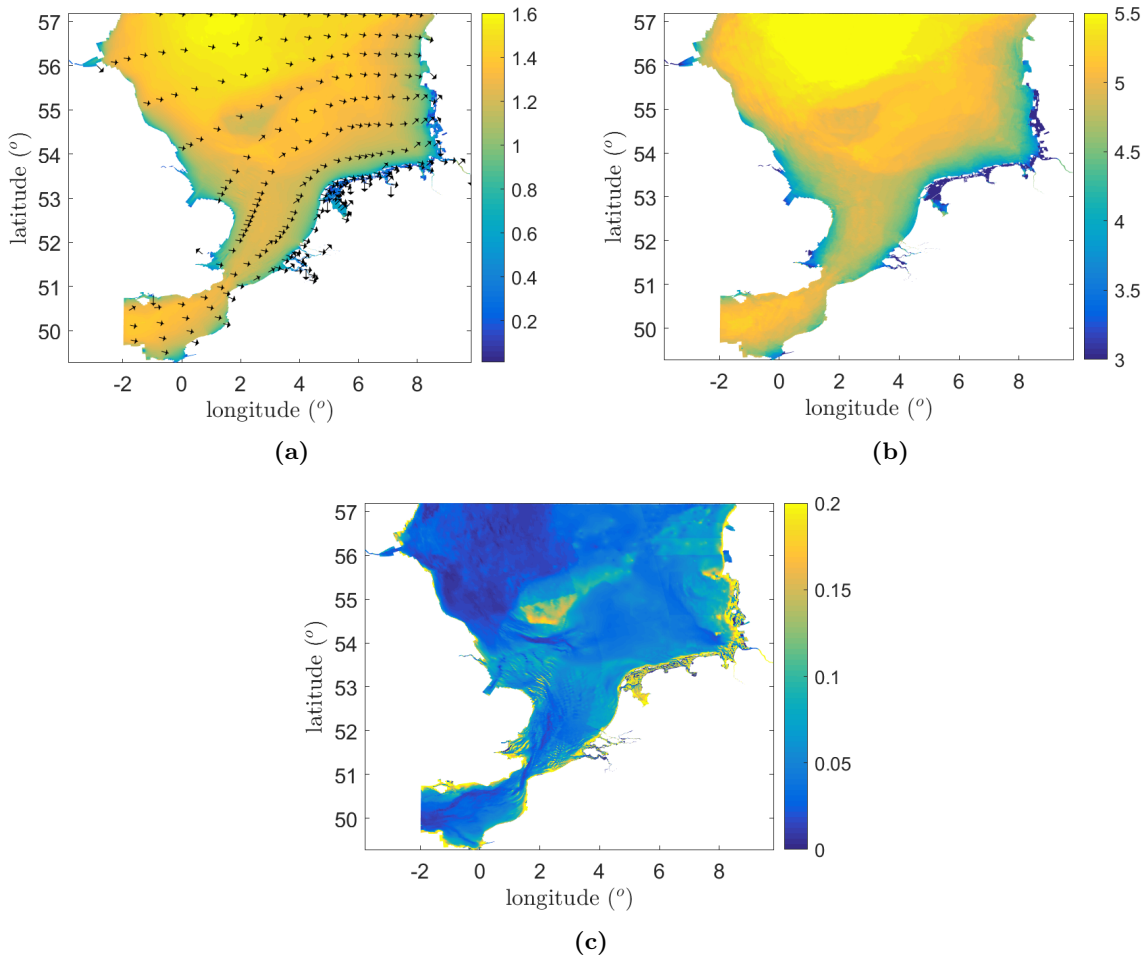

Figure 18: **a** Significant wave height [m] (colors) and wave direction (arrows) calculated from wave scenarios. **b** Peak period [s] calculated from wave scenarios. **c** Root-mean-square amplitude of near bed wave orbital velocity [ms^{-1}] calculated from wave scenarios.

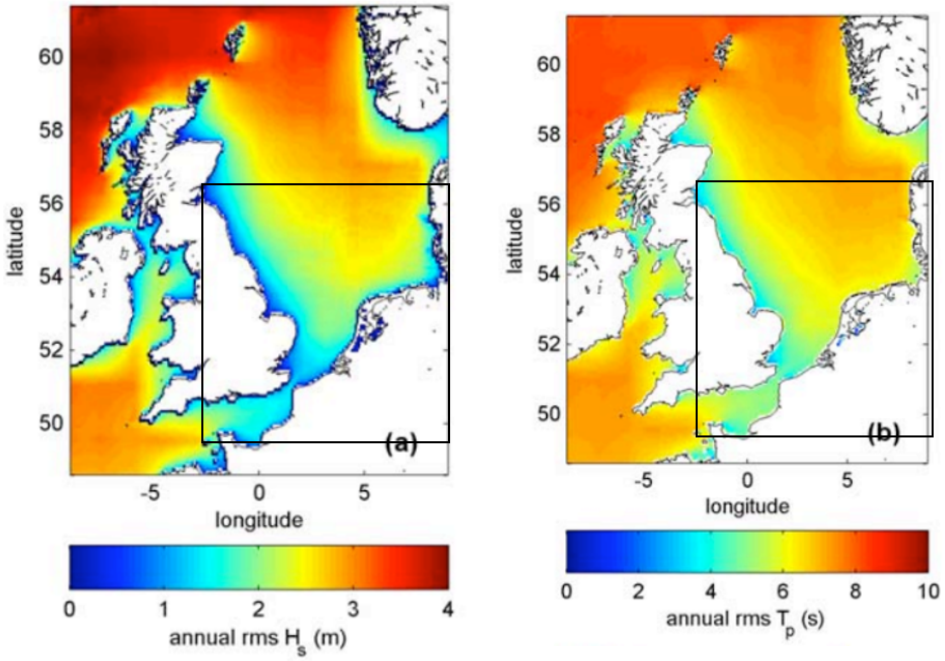

Figure 19: Significant wave height [m] (**a**) and peak period [s] (**b**) by Neill et al. [2009]. The black box represents the ZUNO+ domain.

Table 3: Comparison between model and buoy data, for significant wave height (H_{sig}), peak wave period (T_p) and wave direction (θ). The locations of the buoys can be found in Figure 8.

	H_{sig} [m] observed	H_{sig} [m] modelled	T_p [s] observed	T_p [s] modelled	θ [^{o}] observed	θ [^{o}] modelled
Europlatform	1.26	1.15	5.7	4.6	240	270
Westhinder	1.0	1.17	-	4.7	-	245
Buoy 63110	2.2	1.6	5.8	5.6	-	277
Buoy 62103	1.4	1.3	7.9	5.1	-	277

3.2.2 Influence of sea level rise on the mean wave conditions

The effect of SLR on the wave climate is investigated in a similar way compared to the tides. This means the water depth was increased by 2 m and 10 m, while to coastlines were kept constant. Figure 20 shows the difference between the 2 m SLR and the default case. The significant wave height (Figure 20a) as well as the peak period (Figure 20b) increase with increasing sea level. In Figure 20c the average wave direction of the default case is shown in black and the 2 m SLR case in magenta. There is little to no change in wave direction when the water depth increases. The root-mean-square orbital velocity near the bottom (Figure 20d) decreases over the entire domain, except in the Wadden Sea and near the coast line. The decrease is extra pronounced near features that are closer to the water surface, like the Dogger bank (DB) and the crest of tidal sand ridges (Norfolk banks (NB) and Flemish banks (FB)). These same results are found in the case of 10m SLR, but the difference are larger. These results are presented in the Appendix, Figure A4.

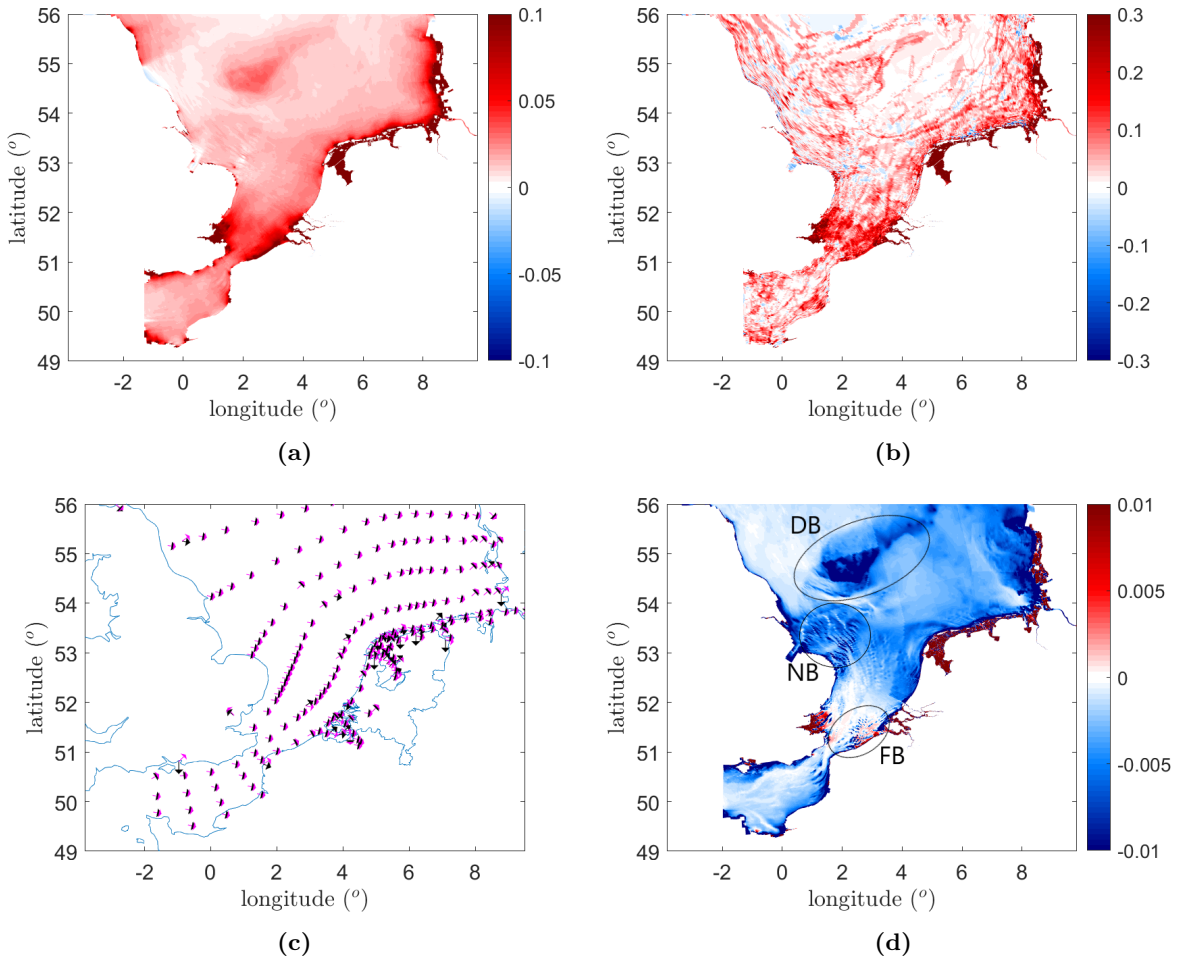

Figure 20: **a** Difference in significant wave height [m], averaged over the different wave scenarios, between 2 m SLR and present-day conditions in the ZUNO+ model. **b** Difference in peak period [s] averaged over the different wave scenarios, between 2 m SLR and present-day conditions in the ZUNO+ model. **c** Wave direction [^{o}] calculated from wave scenarios in the ZUNO+ model, for 2 m SLR (magenta arrows) and present-day conditions(black arrows) **d** Difference in root-mean square orbital velocity near the bottom [ms^{-1}] averaged over the different wave scenarios, between 2 m SLR and present-day conditions in the ZUNO+ model. Figure (**d**) shows the Dogger bank (DB), the Norfolk banks (NB) and the Flemish Banks (FB).

Again, similar to the tides, several runs were done to examine the local effects of SLR on waves on the Belgian shelf, each time with a slightly increasing water depth. The significant wave height, peak wave period, wave direction and orbital velocity are shown in Figure 21. The horizontal axis shows the amount of SLR in m. The significant wave height shows a linear increase with SLR. The peak wave period also increase with SLR, but not entirely linear. The wave direction shows only very slight variations with SLR and will therefore be assumed constant. The orbital velocity at the bottom shows a slight decrease with increasing SLR. This also means that the sediment stirring due to wave motion will slightly decrease with increasing sea level.

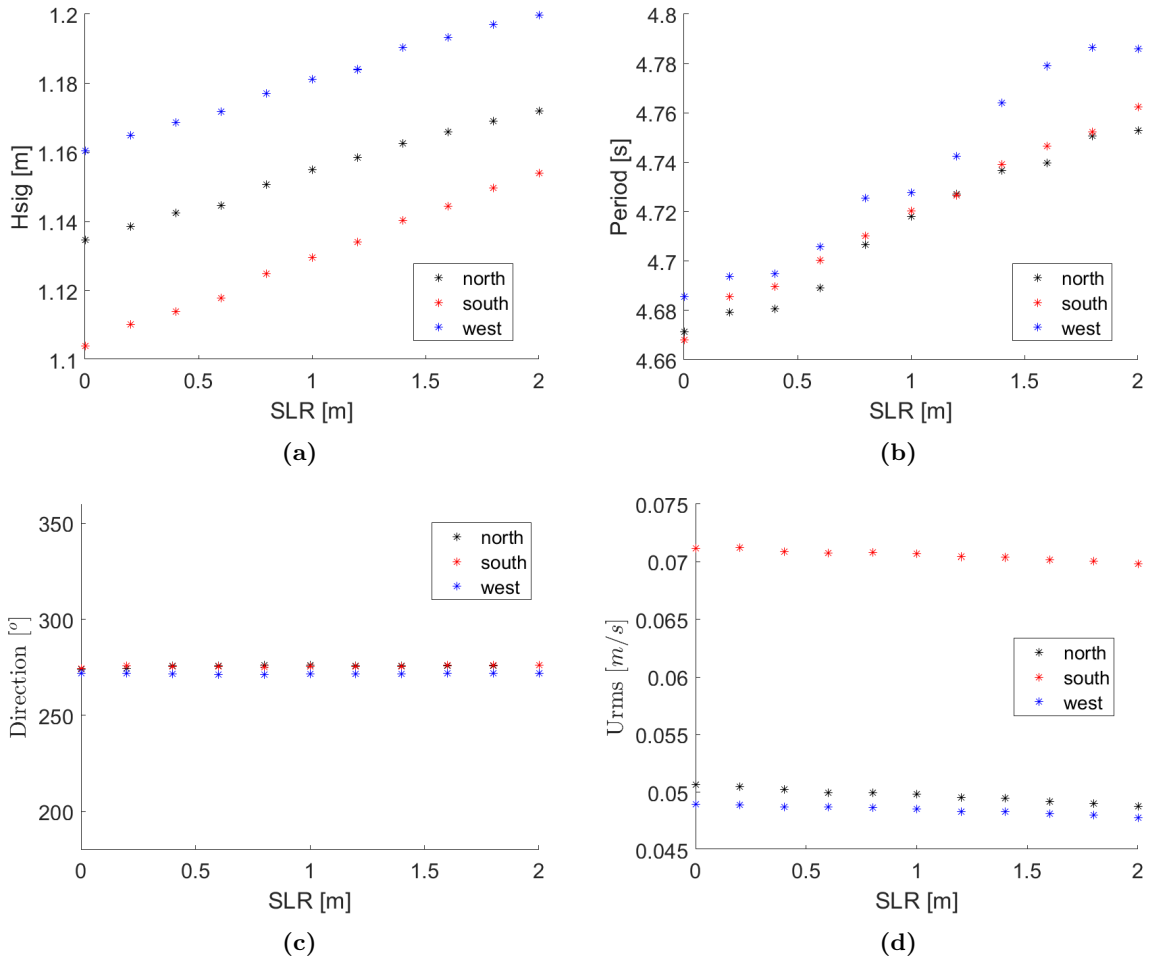

Figure 21: Significant wave height (**a**), peak period (**b**), wave direction (**c**) and orbital velocity at bed (**d**) averaged over each of the Belgian Shelf Model boundaries versus amount of sea level rise.

3.3 Effects of sea level rise on shelf morphodynamics

3.3.1 Present-day conditions

To construct the present-day tidal sand ridges, a spin-up run of 500 years was done. Figure 22 shows snapshots of the model after 0 (**a**), 200 (**b**), 350 (**c**) and 500 years (**d**). The black line in Figure 22d shows the transect over which the cross-section in Figure 23a was taken. Figure 23b shows the same cross-section, but from measured data taken from the EMODnet Bathymetry website. Both the observed and modelled ridges are cyclonically rotated with respect to the tidal current and have a height between 10 and 15 m. There is a difference in the shapes of the troughs, though. The observed ridges have a u-shaped trough, while the modelled ridges have a $v-$shaped trough.

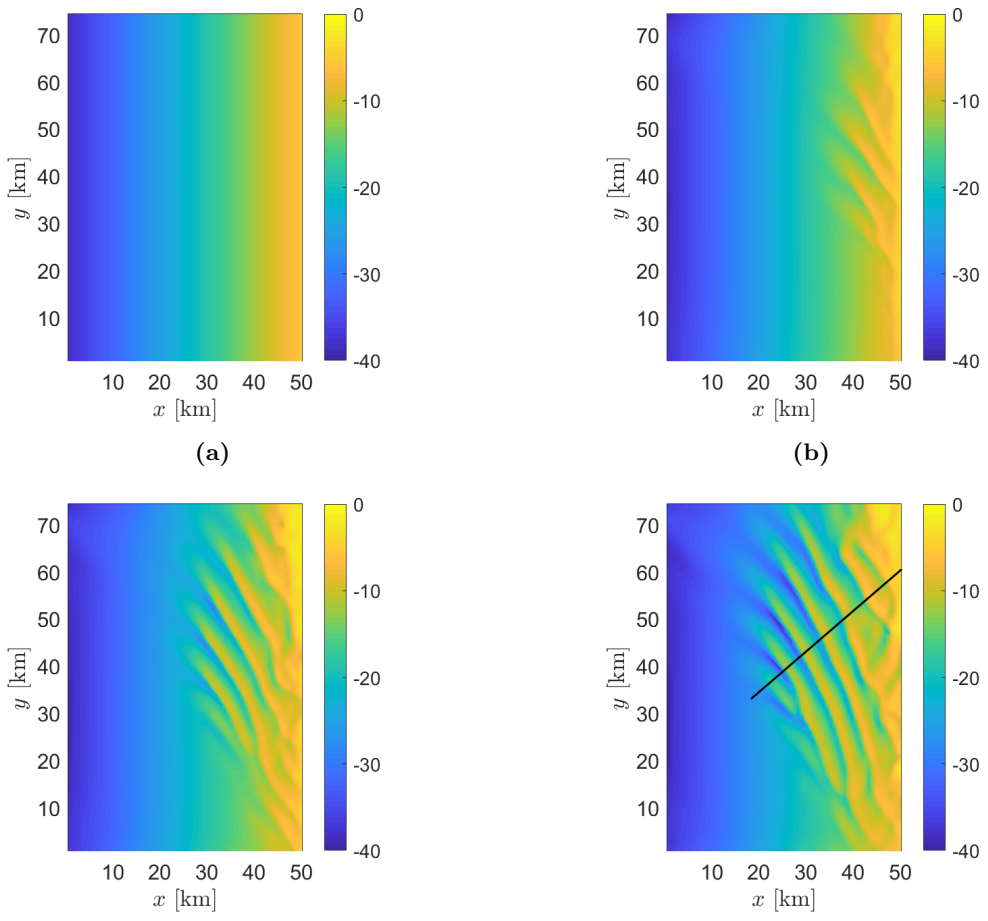

Figure 22: Bed level [m] during the spin-up run for different times, 0 years (a), 200 years (b), 350 years (c) and 500 years (d). Here, x is the cross-shore and y the long-shore coordinate. The coast is on the right and the black line in figure d shows the transect over which cross-sections were made.

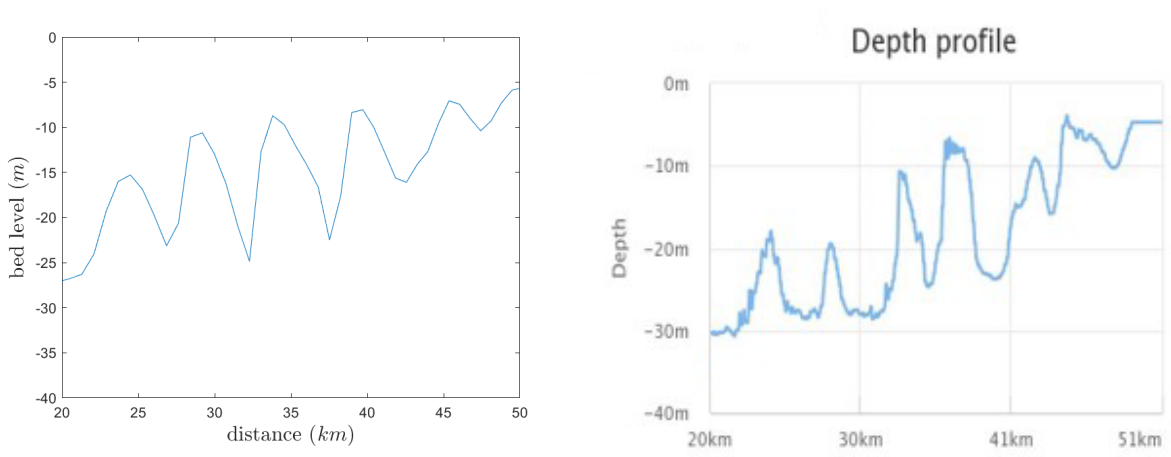

Figure 23: **a** Cross-section of bed level [m] after spin-up along the transect shown in Figure 22d. **b** Cross-section of the measured Belgian shelf along the transect shown in figure 22d. [EMODnet Bathymetry]

3.3.2 Influence of sea level rise with present-day tides and waves

To study the effect of SLR on the tidal sand ridges, 200 years were modelled, starting with the bed level from Figure 22d and adding different rates of SLR. This means that the sea level will increase gradually over time, instead of all at once, like in the tides and waves experiments. Two examples of how the ridges evolve are shown in Figure 24. Both figures show the bed level after 200 years, Figure 24a for 2 mm/yr SLR and Figure 24b for 11 mm/yr SLR, the black lines show the contour levels of the spin-up run after 500 years. Comparing the locations of the crests to the spin-up run shows an offshore migration of the sand ridges. There is also a more pronounced difference between the crests and the troughs visible, when comparing to Figure 22d.

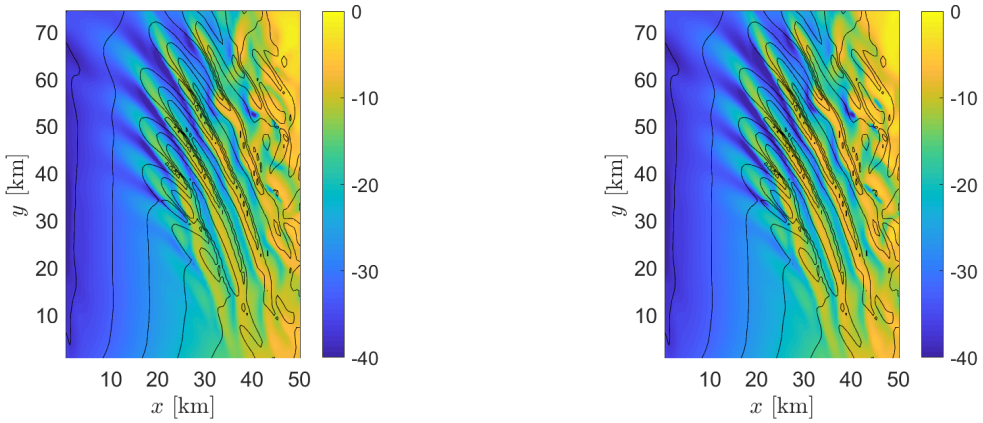

Figure 24: Bed level [m] at 200 years after the spin-up time, with a rate of SLR of 2 mm/yr (**a**) or 11 mm/yr (**b**). The black lines represent the contour lines of the spin-up run after 500 years.

The root-mean-square of the ridge height (h_{rms}) is shown in Figure 25a, for the spin-up run and for the different SLR scenarios. It shows that with a higher the rate of SLR, the ridge height becomes higher. The h_{rms} in Figure 25a is calculated over the full domain, while in Figure 25b only the 20 km closest to the shore are considered. This is where most of the ridges are located (see Figure 22d). Note that the ridge height is higher compared to the full domain. However, the slope is less steep, indicating a slower growth rate. The ratio of the growth rate to SLR rate is shown in Figure 25c. When the ratio is 1 or higher, the ridges can keep up with the rising sea level. When the ratio drops below 1, the ridges are in the risk of 'drowning'. This means in the long term ridges can become quasi-active or even inactive. In this case the ridges can keep up with all the SLR rates, except maybe the 11 mm/yr case, which has a ratio very close to 1. Figure 25d shows the root-mean square ridge height versus the rate of SLR. The ridges grow linearly with the rising sea level.

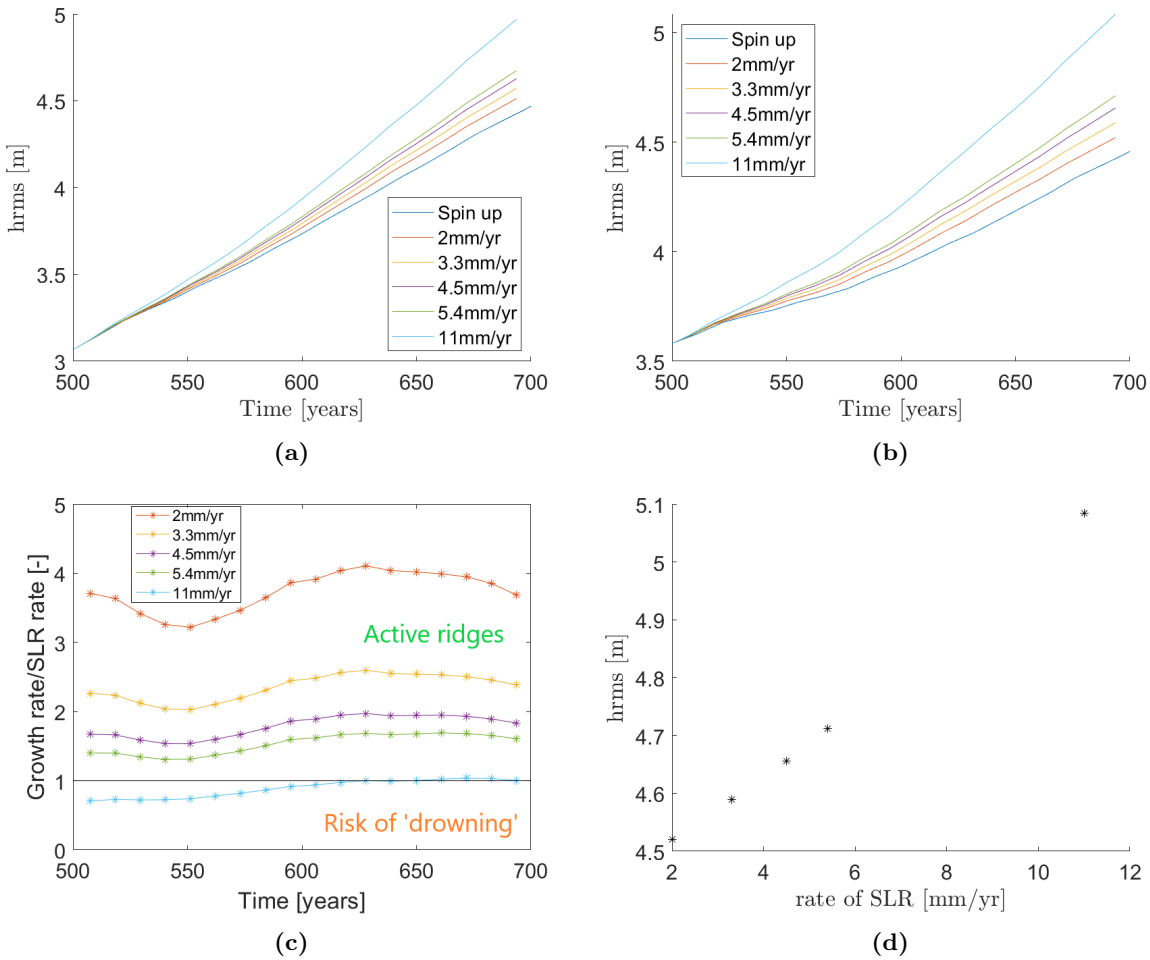

Figure 25: **a** Root-mean square wave height (h_{rms}) of the sand ridges [m] vs time. **b** Root-mean square wave height of the sand ridges [m] vs time, but calculated for the 20 km nearest to the coast (in the x direction). **c** Growth rate of the sand ridges divided by the rate of SLR for the different rates of SLR over the entire domain. Above the value of 1 the ridges will stay active, below 1 there is a risk of 'drowning', meaning the ridges could become quasi-active or inactive. **d** Root-mean square ridge height vs the rate of SLR at 200 years after the spin-up time.

To investigate the source of the sediment that allows the ridges to grow, sediment volume plots were made (Figure 26). The black line shows the volume of sediment in the crest area, the red line shows the volume of trough area (so a negative amount of sediment) and the blue line shows the volume of sediment that passes over the boundaries. The sediment that ends up on the crest originates from the trough, the sediment that does not end up on the crest is transported out of the domain. Figure 26b shows the change in the different volumes versus the rate in SLR. With an increasing rate of SLR the troughs deepen, which leads to the availability of sediment. This available sediment is deposited mostly on the crests. However, the troughs deepen more than the crest are able to grow, which causes a surplus of sediment in the water column. This surplus is transported over the boundaries and lost from the domain. Figure 26c show the residual sediment transport over the entire domain. Figure 26d is the same figure, but zoomed-in on the northern boundary. This shows that the most of the sediment is transported over the crests and through the northern (and southern) boundary.

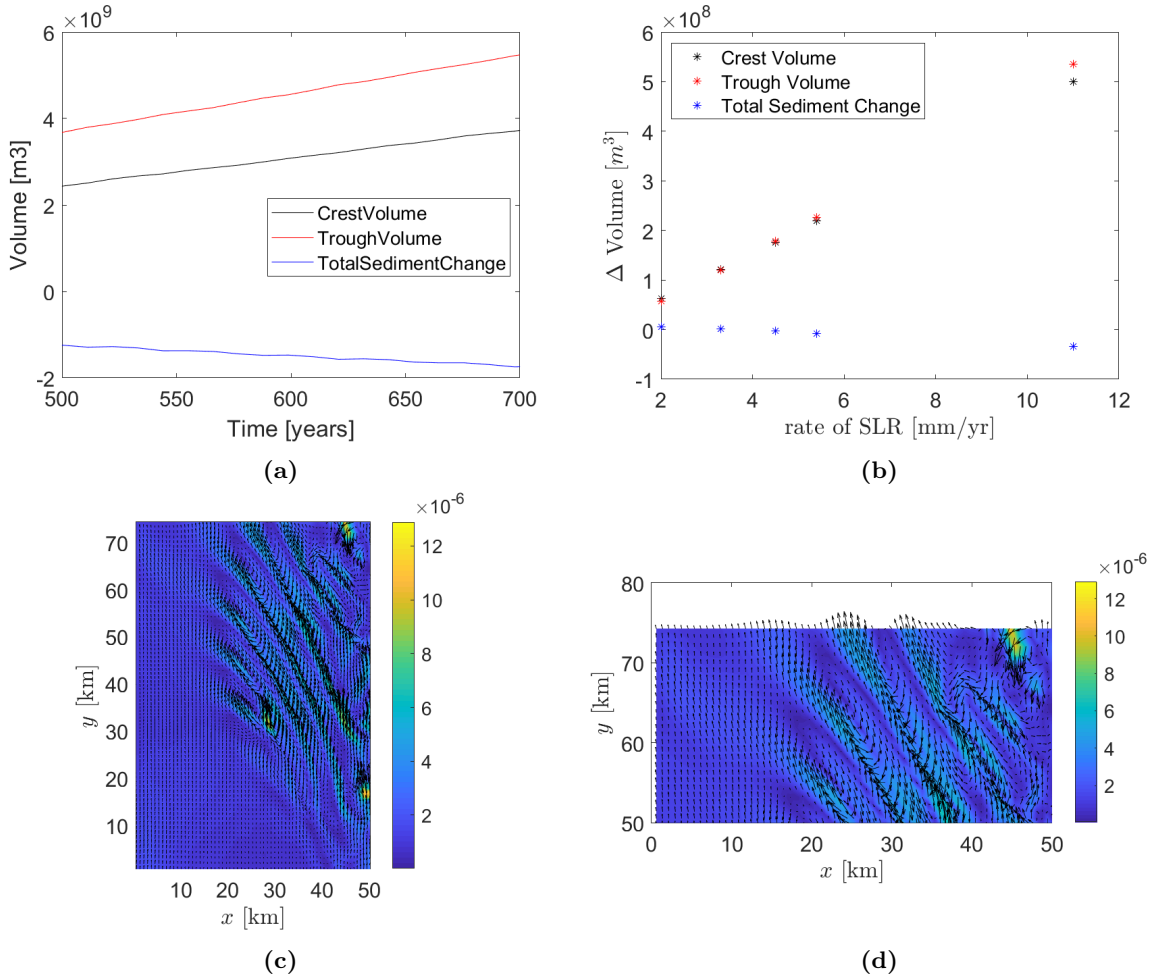

Figure 26: **a** Volumes of the crests, troughs and the amount of sediment that moves over the domain boundaries, for the default case. **b** The change in volumes of the crest, trough and the amount of sediment that moves over the domain boundaries compared to the default case, versus the rate of SLR. **c** The residual sediment transport per unit width in m^2/s. **d** A zoom-in of Figure **c** on the north boundary.

Figure 25 showed that the tidal sand ridges can keep up with a rate of SLR of 11 mm/yr in the modelled 200 year time period. However, since the ratio between the growth rate and the SLR rate is close to 1, a longer run was done to see how the ridges would evolve over a longer time scale. Figure 27a shows on the left axis the root-mean square ridge height over a thousand years, both for the entire domain and for the near shore area. On the right axis the amount of SLR is plotted. Interestingly, the ridges keep on growing with the rising sea level during this entire time period, even though the ratio between the growth rate and the rate of SLR fluctuates around 1 (Figure 27b). The growth of the ridges near the coast is slower compared to the rising sea level, up until 1000 years (500 + 500 years spin-up), when the growth rate increases and the ridges keep pace with the SLR.

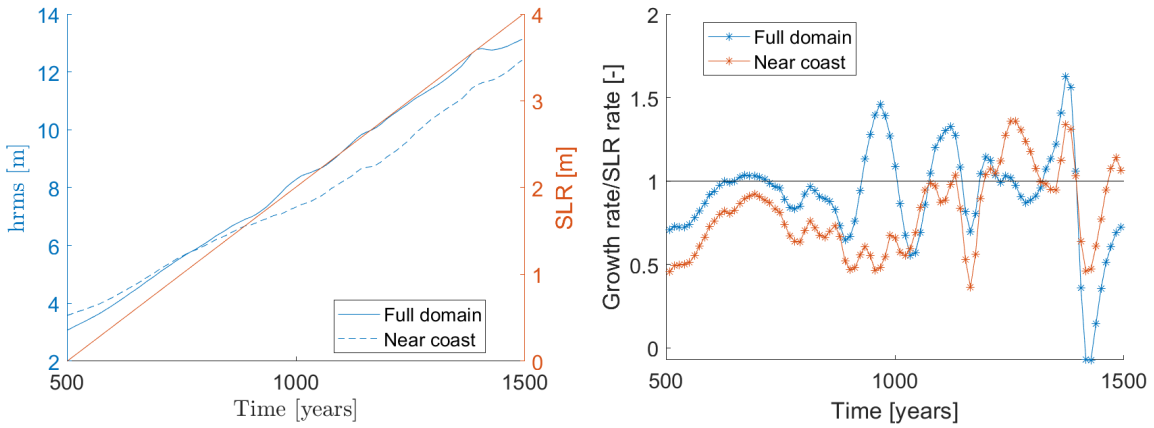

(a) **(b)**

Figure 27: **a** Root mean square ridge height for the 11 mm/yr SLR case, run for 1000 years (+500 years spin-up). The blue line is the h_{rms} for the full domain, while the red line was calculated using only the 20 km nearest to the coast. **b** Ratio between the growth rate and the rate of SLR for the 11 mm/yr SLR case, run for 1000 years. The blue line is the ratio for the full domain, while the red line was calculated using only the 20 km nearest to the coast.

3.3.3 Influence of sea level rise, including sea level rise effects on waves

As seen in chapter 3.2.2, SLR affects the significant wave height and the peak wave period. These changes are now also considered in the morphodynamic runs. Figures 28a and 28b show the bed level after a 200 year run with a rate of SLR of 2 mm/yr and 11 mm/yr, respectively. When comparing these figures to Figure 24, at first glance, there seem very little changes. However, when comparing the cross-sections, (Figures 28c and 28d) a clear shift towards the coast is visible when higher waves are present (yellow versus orange lines). This does not mean that the ridges migrate towards the coast, but that the off-shore migration of the ridges is slowed down due to the waves. This becomes clear when comparing the initial bed level (blue line) to the bed levels after 200 years (orange and yellow lines). Figure 29 shows the ratio between the growth rate of the tidal sand ridges and the SLR rate over the entire domain, similar to Figure 25c, but only for the 11mm/yr SLR case. The blue line shows the results with present-day wave conditions and the orange line shows the results including the effects of SLR on waves. In the first years the increase in significant wave height will make the ridges grow faster. However, over the years, when the water depth has increased more and more, the growth rate slows down and converges with the growth rate of present-day conditions. Both these rates are above 1, so the ridges will not drown.

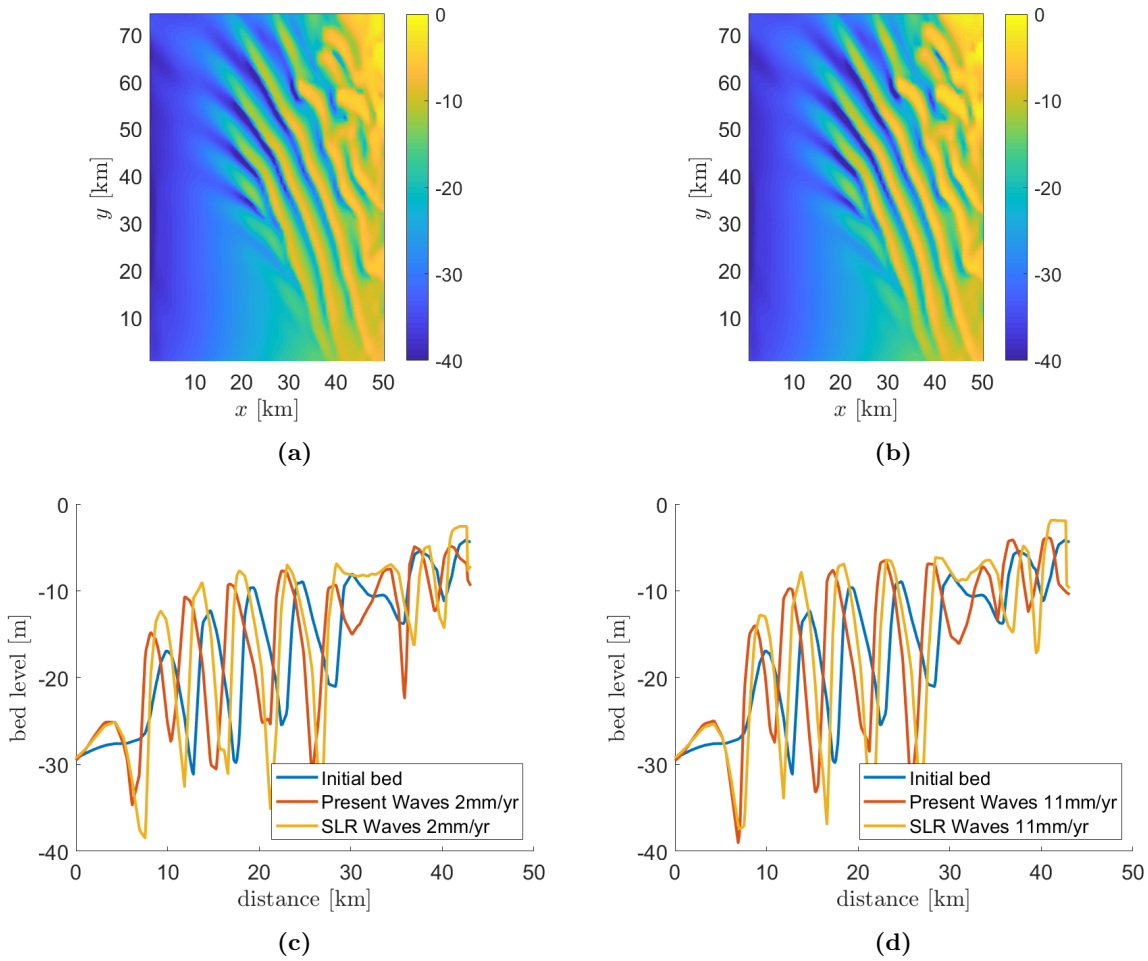

Figure 28: Bed level [m] after 200 years with a SLR rate of 2 mm/yr (**a**) and 11 mm/yr (**b**). Cross-section after 200 years with a SLR rate of 2 mm/yr (**c**) and 11 mm/yr (**d**). The blue line is the initial bed level, the red line uses present-day conditions for waves and the yellow line includes the effects of SLR on waves.

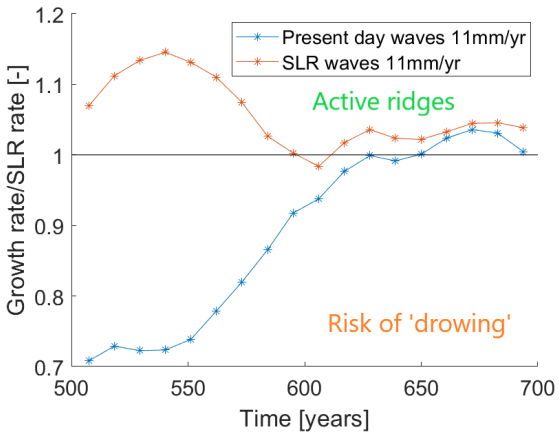

Figure 29: Growth rate of the sand ridges divided by the rate of SLR over the entire domain for the 11mm/yr SLR case. The blue line shows the results with present-day wave condition and the orange line shows the results including the effects of SLR on waves. Above the value of 1 the ridges will remain active, below 1 there is a risk of 'drowning', meaning the ridges could become quasi-active or inactive.

3.3.4 Influence of sea level rise, including sea level rise effects on waves and tides

Finally, in this section results of the morphodynamic runs are shown, in which the effects of SLR on depth, as well on wave forcing and tidal forcing at the boundaries, were included. As was discussed in section 3.1.2, this means an increase in tidal amplitude and a decrease in tidal phase at the boundary of the Belgian Shelf domain. So in these runs the effect of SLR on both tides and waves is taken into account. Figure 30a shows, for the case of 11 mm/yr SLR, the cross-sections of the initial bed level (in blue), the bed level after 200 years with present-day conditions for tides and waves (red) and the bed level after 200 years including the effects of SLR on tides and waves (yellow). The ridges (yellow line) have hardly grown compared to the initial bed. When looking at the ratio of growth rate of the ridges and the SLR rate (see Figure 30b), all the values are well below 1. This indicates that the ridges are not able to keep up with the imposed SLR. However, this does seem unlikely as the tidal sand ridges would not be able to grow even with present-day rates of SLR. Therefore, the ridges are no longer compared to the initial bed level, but to the bed level after a couple of years, to avoid any spin-up problems. These results are shown in Figure 30c. In the case of 11 mm/yr SLR the growth rate is below 1 during the entire period, eventually, these ridges will become inactive. For the other rates of SLR the growth rates do reach values higher than 1, but these rates slowly decline, meaning the ridges are not at risk of 'drowning' yet, but might be on longer time scales.

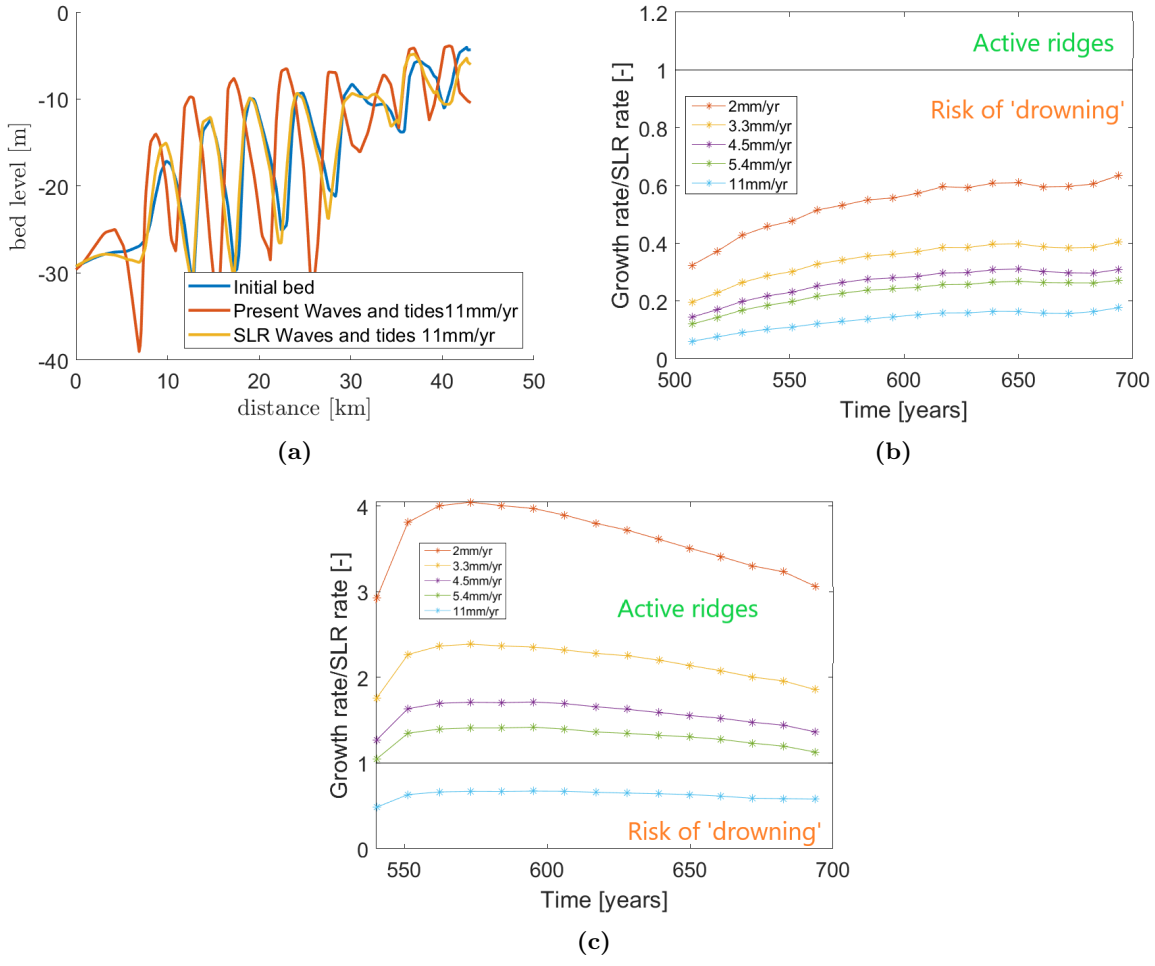

Figure 30: (**a**) Cross-section after 200 years with a SLR rate of 11 mm/yr. The blue line is the initial bed level, the red line uses present-day conditions for waves and tides and the yellow line includes the effects of SLR on waves and tides. (**b**). Growth rate of the sand ridges divided by the rate of SLR over the entire domain for the 11mm/yr SLR case. The blue line shows the results with present-day wave condition the orange line shows the results including the effects of SLR on waves and the yellow line shows the results including the effects of SLR on both waves and tides. Above the value of 1 the ridges will remain active, below 1 there is a risk of 'drowning', meaning the ridges could become quasi-active or inactive.

4 Discussion

4.1 Effects of sea level rise on tides

This study extends earlier work by Pickering et al. [2012] and Schindelegger et al. [2018] and examines the effect of SLR on the tide in the North Sea. Similar to what is in those papers the changes in M_2 sea surface amplitude and phase are assessed, but in addition also the changes in tidal current and in the residual M_0 and first overtide M_4. The model used is state-of-the-art and has a high resolution bathymetry. Overall, it was found that the model accurately represents the tidal constituents in the North Sea. Nevertheless, some differences were found between the modelled results and the results by Pickering et al. [2012] (Figure 13 and 14, respectively). Both show a change in M_2 amplitude in the same order of magnitude and a shift in the amphidromic points. The location of these points is different, though. This could be explained by a difference in forcing (Pickering et al. [2012] forces only with the M_2 tide, while this study uses the astronomical tide, which includes many constituents), but also by the improved quality of the model used in this study. A sensitivity analysis on the shift in amphidromic points could be done to find out which variable is the most important contributor. Despite these differences, the conclusion by Pickering et al. [2012] that the changes in tidal characteristics are non-linearly with SLR still stands. The shifting of the amphidromic points leads to a non-linear change in tidal amplitude. However, when looking specifically at the boundaries of the Belgian Shelf Model, it was found that the M_2 tidal amplitude increases (and the phase decreases) more or less linearly with SLR. The M_2, M_4 and M_0 current velocities all decrease with SLR, which leads to a decrease in sediment stirring.

4.2 Effects of sea level rise on waves

As mentioned in section 2.1.2, the waves in the model are generated in the large-scale DCSM domain by wind. A downside of this approach is that only the effects of wind waves is investigated, thereby ignoring the effects of swell waves. The reason behind this is that the model could not cope with an input for swell waves and wind waves at the same time. A study on swell waves by Amores and Marcos [2020] finds that the number of swell events will likely decreases in the future. With the influence of swell waves decreasing over time, the assumption of only modelling wind wave becomes slightly more valid. Nevertheless, the lack of swell waves is the reason that the modelled data does not completely match the observed data.

Another limitation is that, to construct the wave climate, realisations are performed for different wind speeds and directions, where the wind and the probability distribution over the different winds are considered to be spatially uniform. Thus, it is expected that this approach does not properly account for the effects of changing pressure fields. To achieve that, the model should be forced with time series of the wind, as is done in Neill et al. [2009] and Bricheno and Wolf [2018].

The third limitation of this study is that the probabilities used to construct the average wave conditions are kept the same when sea level changes. According to Debernard and Røed [2008] the frequency of storm surges will increase over the southeastern North Sea. If this would have been taken into account the probabilities for the storm scenarios would have been increased. As storm surges are linked to high significant wave height, including this effect would have lead to an even higher increase in significant wave height with SLR.

What is new in this study, compared to previous studies [Neill et al., 2009, and others] is examining the effects of SLR on the wave orbital velocity near the bed. This is important quantity for coastal morphodynamics, as it induces stirring of sediment from the bottom. Soulsby [1998] defined the amplitude of the wave orbital velocity as follows:

$$U_w = \frac{\pi H_{sig}}{T \sinh(kh)}. \tag{15}$$

Here, H_{sig} is the significant wave heigth, T the wave period, k the wavenumber and h the water depth. So, both the water depth and the height of the waves influences the value for U_w. This is seen in Figure 20d, where the increasing water depth leads to a decreasing near bed wave orbital velocity throughout most of the domain. The only areas where the wave orbital velocity increases is in the coastal areas where the increase in significant wave height with SLR is high.

4.3 Effects of sea level rise on shelf morphodynamics

The Belgian Shelf Model models the tidal sand ridges on the Belgian shelf. The model extends the study of Nnafie et al. [2020] in the sense that it accounts for changes in mean sea level. It does so in three ways: changes in depths, changes in tidal forcing and changes in wave forcing at the boundaries. Effects of changes in mean sea level on the evolution of tidal sand ridges were also assessed by Yuan and De Swart [2017]. However, the present model is more realistic. First, it considers a sloping shelf bounded by a coast, instead of a domain with open boundaries in which the mean depth is constant. Second, it accounts for phase differences of the tide over the domain, which are ignored by Yuan and De Swart [2017]. And third, rather than using highly schematized formulations for waves and sand transport, this model employs state-of-the-art formulations for these variables.

Figure 23 shows the cross-section of the model run and the cross-section of the measured bathymetry. The cross-sections look similar, both show five main ridges with a depth between 5 and 30 meters. However, there are also some differences. The troughs are more sharply defined in the model run and the location of the ridges is also slightly different. A reason for this could be that the ridges were still growing as the spin-up run (in which the mean sea level was fixed and which lasted 500 years) was not yet in a steady state. In the modelled 200 years after the spin-up the tidal sand ridges can kept with the rising sea level, even under the most extreme case of 11 mm/yr. The sediment to keep the crests growing originates from the troughs, as can be seen in Figure 26. This figure also shows that sediment is lost over the boundary. Figure 26c shows that this sediment is lost over the north boundary.

From Figure 25c it seems that 11 mm/yr SLR causes the ridges not to keep pace with SLR over a longer time period. This case was modelled for 1000 years, which is shown in Figure 27. Clearly, the tidal sand ridges grow with the sea level as long as there is a sediment supply. This sediment supply from the troughs will cease if the critical velocity for erosion is no longer reached in the troughs. According to Miller et al. [1977] and Soulsby [1998] the critical velocity for sediment with a grain size of 0.2 mm is 4 cm/s. Figure 21d shows that the orbital velocity at the bed does not fall below this value if the sea level rises up to 2 m. When, the effects of SLR on waves are included, the significant wave height increases with ≈ 4 cm. This small increase is enough to decrease the offshore migration of the tidal sand ridges. This could be due to the decrease in orbital velocity near the bed, which leads to less sediment stirring. When the effects on tides are implemented as well, there seems to be a spin-up problem, as the ridges cannot keep up even with present-day values for SLR. When the first years are removed from the dataset, more realistic results are found. This time, only the ridges in the most extreme case of SLR are unable to keep pace. Nevertheless, the ratio between growth rate and SLR rate decreases over time for all scenarios. This could be expected, as the tidal current velocities for both the M_2, M_4 and M_0 constituents is reduced with an increased water depth, which also leads to a decrease in sediment stirring. To know for sure if the tidal sand ridges can keep pace with the smaller rates of SLR, longer runs have to be done. Similar to the 1000 year run with present-day conditions for tides and waves.

There are several simplifying assumptions in the Belgian shelf model. One of them is that with increasing sea level the location of the boundary between shelf and coastal area is kept fixed. In other words, when sea level rises, the entire shelf gets deeper. In reality, with increasing sea level the shelf extends landward and, without hard protection works, the coastline would retreat. Another limitation is that the nearshore zone, where waves break, is not explicitly modelled. Consequently, there is no feedback between what happens on the shelf and what occurs near the coast. These would be interesting topics for future research.

Tidal sand ridges have an important role in coastal protection, for example by dissipating wave energy. The future evolution of these ridges is of great interest for coastal management. This study shows that the ridges can keep up high levels of SLR, as long as there is sediment available, but in extreme cases they will become inactive. As tidal sand ridges are a favoured location for sand extraction (used for beach nourishment) and the troughs cannot keep deepening infinitely, the sediment supply may at some point no longer be enough. If this would happen and the ridges would be come quasi-active or even inactive, this would have severe consequences for the coastal zones located behind these ridges. Therefore, with the rising sea level the growth of the tidal sand ridges should be monitored. When extracting sand it should be taken into consideration not to disrupt the sediment supply to the crests. Overall, extreme cases of SLR should be mitigated.

5 Conclusions

The impact of sea level rise on tides, waves in the North Sea and tidal sand ridges on the Belgian shelf has been modelled using the state-of-the-art morphodynamic model Delft3D. The model was found to accurately model the present-day M_2 and M_4 tidal constituents of sea surface height an velocity, as well as the residual current, in the North Sea. When implementing SLR the impact on the amplitudes and phases of these constituents was investigated. It was found that the tidal range increases along the Dutch and Belgian coast, as well as in the English Channel. However, along the eastern UK coast the tidal range decreases. With increasing water depth, the tidal wave was found to propagate faster. The tidal current increases along most of the Belgian, Dutch and Danish coast, but decreases along the British coast.

Furthermore, the effect of SLR on the significant wave height, the peak period, the wave direction and the orbital velocity at the bed in the North Sea was investigated. The significant wave height was found to increase throughout the entire North Sea, but especially over ridges such as the Dogger Bank and near the coasts. The peak wave period also increases throughout the domain, while the wave direction stays constant. The wave orbital velocity, which causes stirring of sediment, mainly decreases, specifically over crests of ridges like the Dogger bank and the Norfolk banks. However, it increases near the coast and in the Wadden Sea, at all these locations the significant wave height was higher than the rest of the domain, indicating that the increasing wave height offsets the effects of the increasing water depth.

Zooming in onto the Belgian shelf, where the tidal sand ridges are modelled, it was found that the tidal amplitude increases almost linearly with SLR, while the tidal phase decreases almost linearly. A decreasing phase indicates an earlier arrival of the tidal wave at a certain location and therefore a faster travelling wave. The tidal currents of the M_2, M_4 and M_0 all decrease with a rising sea level. As for the waves, both the significant wave height and the peak period increase with an increasing sea level. The wave direction stays more or less constant and the wave orbital velocity decreases slightly. The decrease in wave orbital velocity and tidal currents will lead to less sediment stirring.

Next, the effect of SLR on the evolution of tidal sand ridges was studied in three different ways. In the first series of experiments, only depth was changed and present-day conditions for tides and waves at the open boundaries of the domain were imposed. After a spin-up period of 500 years, in which the mean sea level was kept fixed, different rates of SLR were considered (up to 11 mm/yr). The tidal sand ridges were found to keep pace with SLR for the next 200 years for all rates of SLR. For the most extreme SLR scenario the tidal sand ridges were modelled for 1000 years and even then they grew along with the rising sea level. The sediment needed for the ridges to keep growing originates from the troughs. However, not all the available sediment is deposited on the crests, a small part is transported over (mainly) the northern boundary out of the domain. In the second series of morphodynamic experiments, SLR affected both depth and wave forcing, while tidal forcing was still maintained at present-day conditions. In this case it turned out that the offshore migration of the tidal sand ridges is reduced, meaning that they will stay closer to the coast for a longer period of time, offering better coastal protection. In the third series of experiments, SLR affected the water depth, wave forcing and tidal forcing. In this case the tidal sand ridges were found to no longer grow with SLR, when the rate is 11 mm/yr. For the other cases the ridges are able to keep pace with the rising sea level. However, the growth rate decreases over time, which might lead to implications in the future.

For future coastal protection, the growth of the tidal sand ridges should be monitored. When extracting sand it should be taken into consideration not to disrupt the sediment supply to the crests and extreme cases of SLR should be mitigated.

Acknowledgments

I would like to thank the UK Met Office and Centre for Environmental Data Analysis for providing me with the necessary buoy data. I would also like to thank Huib and Abdel for keeping me motivated throughout the process of writing this thesis, even when social distancing. Finally, I would also like to thank my family for all the working-from-home-days spent together, and Christian, for his never wavering trust in me.

References

A. Amores and M. Marcos. Ocean swells along the global coastlines and their climate projections for the twenty-first century. *Journal of Climate*, 33(1):185–199, 2020. doi: 10.1175/JCLI-D-19-0216.1.

T.J. Andersen, J. Fredsoe, and M. Pejrup. In situ estimation of erosion and deposition thresholds by acoustic doppler velocimeter (adv). *Estuarine, Coastal and Shelf Science*, 75(3):327 – 336, 2007. doi: https://doi.org/10.1016/j.ecss.2007.04.039.

R.H. Belderson, R.D. Pingree, and D.K. Griffiths. Low sea-level tidal origin of celtic sea sand banks — evidence from numerical modelling of m2 tidal streams. *Marine Geology*, 73(1):99 – 108, 1986. doi: https://doi.org/10.1016/0025-3227(86)90113-1.

N. Booij, L. H. Holthuijsen, and R. C. Ris. *'SWAN' wave model for shallow water.* 1997. doi: doi/abs/10.1061/9780784402429.053.

L.M. Bricheno and J. Wolf. Future Wave Conditions of Europe, in Response to High-End Climate Change Scenarios. *Journal of Geophysical Research: Oceans*, 123(12):8762–8791, 2018. doi: 10.1029/2018JC013866.

J.A. Church, P.U. Clark, A. Cazenave, J.M. Gregory, S. Jevrejeva, A. Levermann, M.A. Merrifield, G.A. Milne, R.S. Nerem, P.D. Nunn, A.J. Payne, W.T. Pfeffer, D. Stammer, and A.S. Unnikrishnan. *Sea level change.* Cambridge University Press, Cambridge, United Kingdom and New York, NY, USA, 2013. ISBN 9780128130810. doi: 10.1016/B978-0-12-409548-9.10820-6.

D.L. Codiga. Unified Tidal Analysis and Prediction Using the UTide Matlab Functions. Technical report, 2011.

A.M. Davies and G.K. Furnes. Observed and Computed M2 Tidal Currents in the North Sea. *Journal of Physical Oceanography*, 10(2):237–257, feb 1980. doi: 10.1175/1520-0485(1980)010¡0237:OACMTC¿2.0.CO;2.

H.E. De Swart and B. Yuan. Dynamics of offshore tidal sand ridges, a review. *Environmental Fluid Mechanics*, 19:1047–1071, 2019. doi: 10.1007/s10652-018-9630-8.

J.B. Debernard and L.P. Røed. Future wind, wave and storm surge climate in the Northern Seas: A revisit. *Tellus, Series A: Dynamic Meteorology and Oceanography*, 60 A(3):427–438, 2008. doi: 10.1111/j.1600-0870.2008.00312.x.

Deltares. Delft3D-FLOW User Manual, May 2019a.

Deltares. Delft3D-WAVE User Manual, May 2019b.

M.W. Dingemans, A.C. Radder, and H.J. De Vriend. Computation of the driving forces of wave-induced currents. *Coastal Engineering*, 11(5):539 – 563, 1987. doi: https://doi.org/10.1016/0378-3839(87)90026-3.

K.R. Dyer and D.A. Huntley. The origin, classification and modelling of sand banks and ridges. *Continental Shelf Research*, 19:1285–1330, 1999. doi: 10.1016/S0278-4343(99)00028-X.

EMODnet Bathymetry. Understanding the topography of the european seas. URL `https://portal.emodnet-bathymetry.eu/?menu=19`. Accessed on 01-06-2020.

Flanders Hydraulics Research, Antwerp.

Peng Gao. A general bedload transport equation for homogeneous grains. 2010. URL `https://serc.carleton.edu/48147`. Accessed on 06-07-2020.

C Gautier and S Caires. Operational wave forecasts in the southern north sea. In *36th IAHR World Congress, 28th June–3 July*, volume 1, page 5, 2015.

T. Gerkema. Tides in Coastal Seas and Basins. *An Introduction to Tides*, 122:122–156, 2019. doi: 10.1017/9781316998793.007.

J.M. Huthnance. On one mechanism forming linear sand banks. *Estuarine, Coastal and Shelf Science*, 14(1):79 – 99, 1982. doi: doi.org/10.1016/S0302-3524(82)80068-6.

G R Lesser, J A Roelvink, J.A.T.M. van Kester, and G S Stelling. Development and validation of a three-dimensional morphological model. *Coastal Engineering*, 51(8):883–915, 2004. doi: https://doi.org/10.1016/j.coastaleng.2004.07.014.

Z. Liu, Y. Ping, Y. Xiong, S. Berne, T. Alain, and C. Li. Quaternary transgressive and regressive depositional sequences in the east china sea. *Chinese Science Bulletin*, 48:81–87, 06 2003. doi: 10.1007/BF02900944.

J.L. Merkens, L. Reimann, J. Hinkel, and A.T. Vafeidis. Gridded population projections for the coastal zone under the shared socioeconomic pathways. *Global and Planetary Change*, 145:57 – 66, 2016. doi: https://doi.org/10.1016/j.gloplacha.2016.08.009.

M.C. Miller, I.N. McCave, and P.D. Komar. Threshold of sediment motion under unidirectional currents. *Sedimentology*, 24(4):507–527, 1977.

S.P. Neill, J.D. Scourse, G.R. Bigg, and K. Uehara. Changes in wave climate over the northwest European shelf seas during the last 12,000 years. *Journal of Geophysical Research: Oceans*, 114, 2009. doi: 10.1029/2009JC005288.

A. Nnafie, T.B.J. Wolf, and H.E. De Swart. Tidal sand ridges on the shelf : A numerical study of their natural morphodynamic evolution and response to interventions. *Continental Shelf Research*, 205, 2020. doi: doi.org/10.1016/j.csr.2020.104195.

M.D. Pickering, N.C. Wells, K.J. Horsburgh, and J. A.M. Green. The impact of future sea-level rise on the European Shelf tides. *Continental Shelf Research*, 35:1–15, 2012. doi: 10.1016/j.csr.2011.11.011.

D. Prandle. Residual Flows and Elevations in the Southern North Sea. *Proceedings of The Royal Society A: Mathematical, Physical and Engineering Sciences*, 359:189–228, 1978. doi: 10.1098/rspa.1978.0039.

J.Y. Reynaud and R. Dalrymple. *Shallow-Marine Tidal Deposits*, pages 335–369. 01 2012. doi: 10.1007/978-94-007-0123-6$_1$3.

J.A. Roelvink. Coastal morphodynamic evolution techniques. *Coastal Engineering*, 53(2):277–287, 2006. doi: https://doi.org/10.1016/j.coastaleng.2005.10.015.

J.A. Roelvink and D. Walstra. Keeping it simple by using complex models. *Advances in Hydro-science and Engineering*, 6:1–11, 2004.

J.A. Roelvink, T. Van der Kaaij, and B.G. Ruessink. Calibration and verification of large-scale 2d/3d flow models, phase 1. 11, 2001.

P.C. Roos, S.J.M.H. Hulscher, M.A.F. Knaapen, and R.M.J. Van Damme. The cross-sectional shape of tidal sandbanks: Modeling and observations. *Journal of Geophysical Research: Earth Surface*, 109, 2004. doi: 10.1029/2003JF000070.

M. Schindelegger, J.A.M. Green, S.B. Wilmes, and I.D. Haigh. Can We Model the Effect of Observed Sea Level Rise on Tides? *Journal of Geophysical Research: Oceans*, 123:4593–4609, 2018. doi: 10.1029/2018JC013959.

R. Soulsby. *Dynamics of Marine Sands: A Manual for Practical Applications*. Thomas Telford Publications, London, 1998. ISBN 978072772584X.

J. Van de Kreeke and K. Robaczewska. Tide-induced residual transport of coarse sediment; application to the ems estuary. *Netherlands Journal of Sea Research*, 31(3):209 – 220, 1993. doi: ttps://doi.org/10.1016/0077-7579(93)90022-K.

L.C. Van Rijn. Sediment transport, part ii: Suspended load transport. *Journal of Hydraulic Engineering*, 110(11):1613–1641, 1984. doi: 10.1061/(ASCE)0733-9429(1984)110:11(1613).

L.C. Van Rijn et al. *Principles of sediment transport in rivers, estuaries and coastal seas*, volume 1006. Aqua publications Amsterdam, 1993.

G.K. Verboom, J.G. de Ronde, and R.P. van Dijk. A fine grid tidal flow and storm surge model of the north sea. *Continental Shelf Research*, 12(2):213 – 233, 1992. doi: https://doi.org/10.1016/0278-4343(92)90030-N.

T. Wolf. *Modelling shelf morphodynamics and shoreline change : free behaviour and response to the construction of artificial islands*. PhD thesis, Utrecht Univerisity, 2019.

B. Yuan and H.E. De Swart. Effect of sea level rise and tidal current variation on the long-term evolution of offshore tidal sand ridges. *Marine Geology*, 390:199–213, 2017. doi: 10.1016/j.margeo.2017.07.005.

6 Appendix

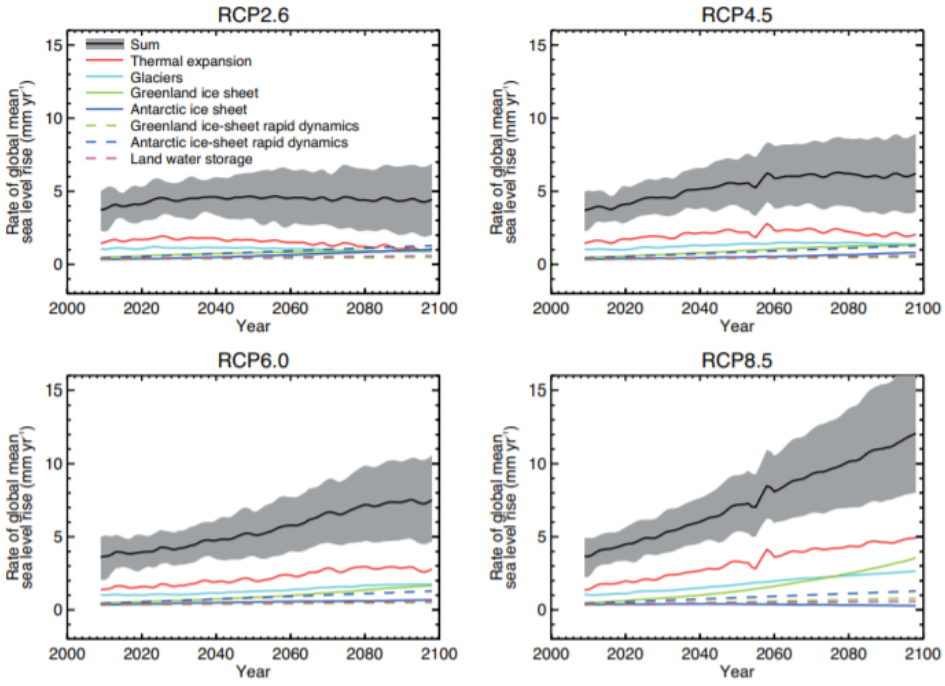

Figure A1: Projections of global mean rate of sea level rise and its contributors for different IPCC scenarios. [Church et al., 2013]

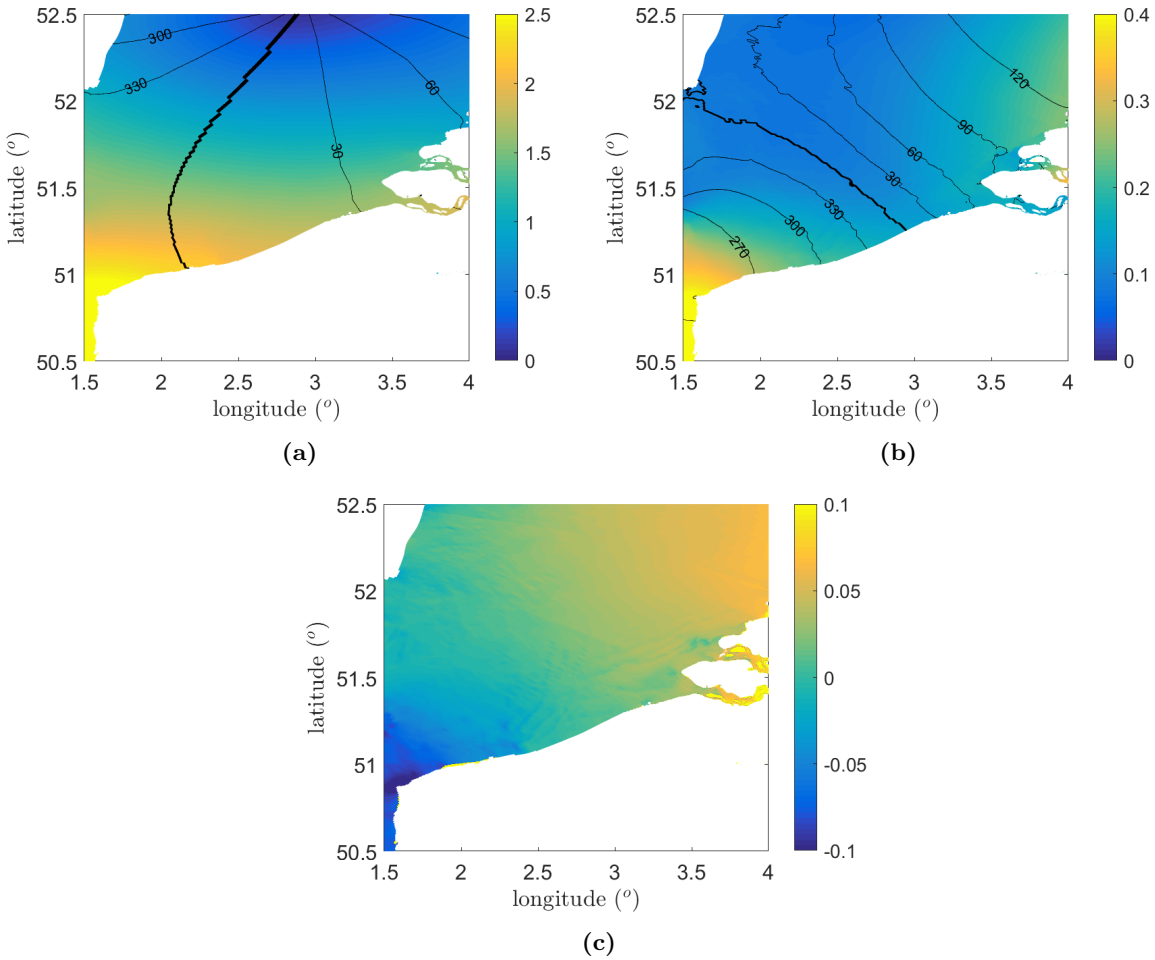

Figure A2: **a** Zoom-in of Figure 10a. M2sea surface elevation computed by the ZUNO+ model for present-day conditions inthe Southern North Sea. Black lines represent tidal phase in degrees, the colors represent tidal amplitudein m. **b** Zoom-in of Figure 11a. M4tidal constituent in the ZUNO+ model for present day conditions. Colors representthe water level in m and the black lines represent the phase in degrees. **c** Zoom-in of Figure 11b. M0tidal constituent in the ZUNO+model for present day conditions. Colors represent the water level in meters.

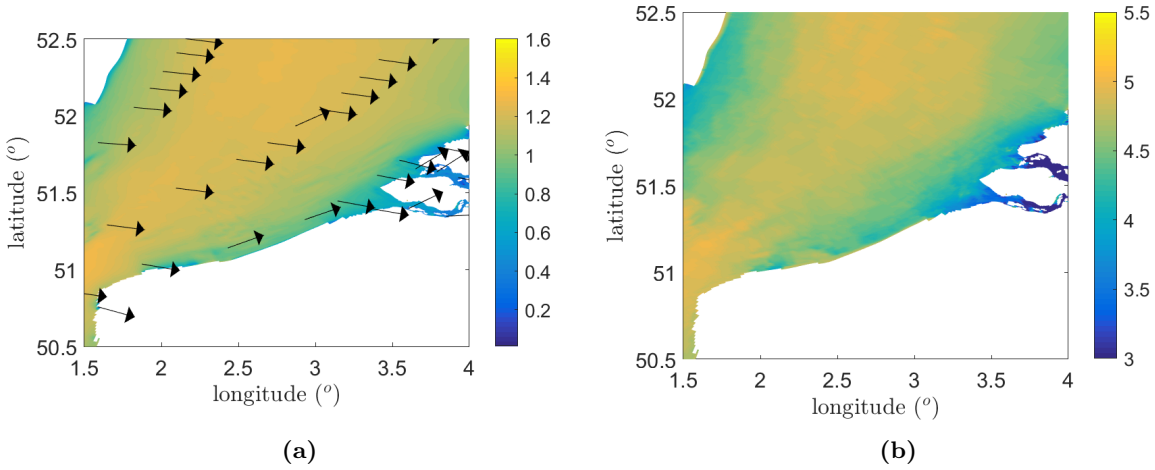

Figure A3: **a** Zoom-in of Figure 18a. Significant wave height [m] (colors) and wave direction (arrows) calculated from wave scenarios.**b** Zoom-in of Figure 18b. Peak period [s] calculated from wave scenarios.

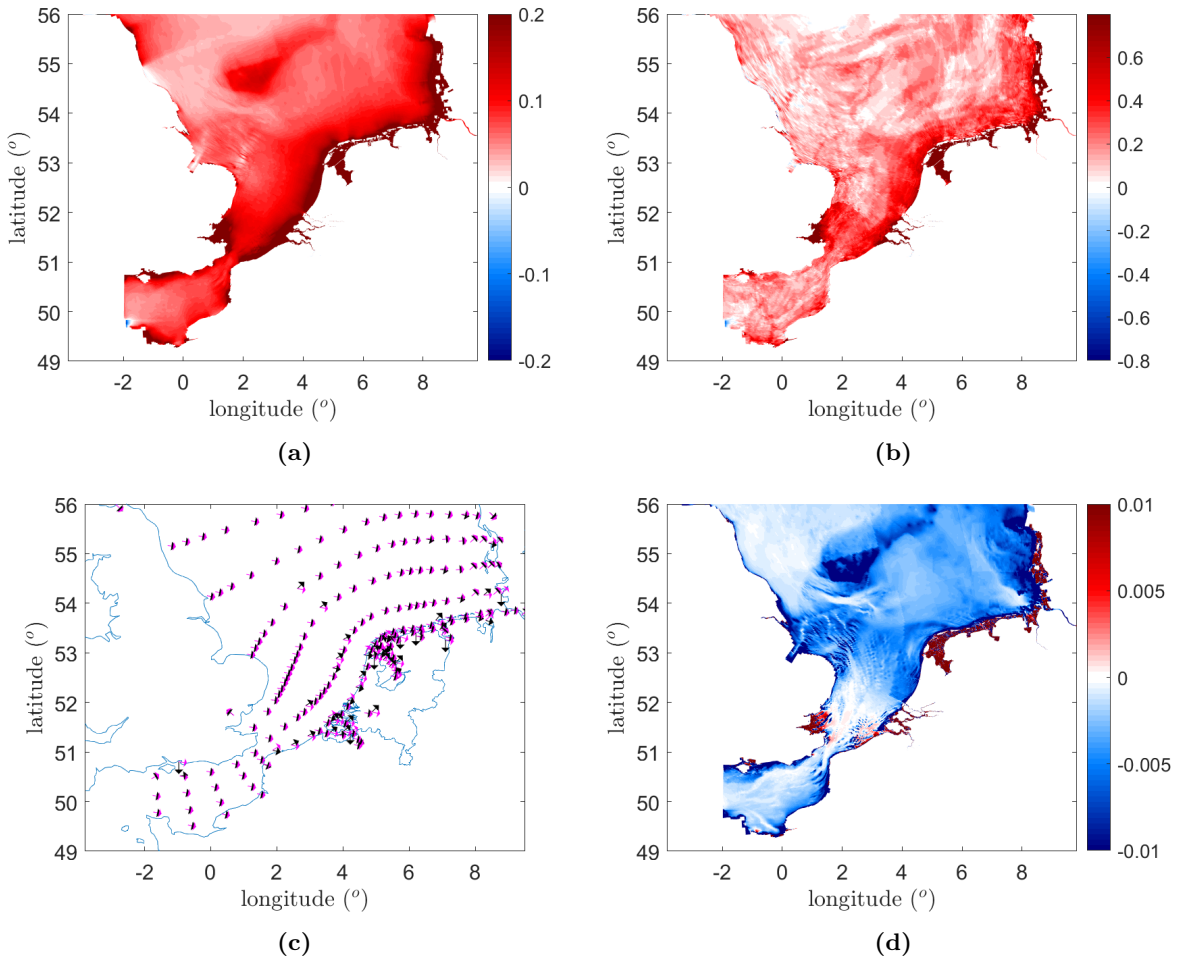

Figure A4: **a** Difference in significant wave height [m] calculated from wave scenarios, between 2m SLR and present day conditions in the ZUNO+ model. **b** Difference in peak period [s] calculated from wave scenarios, between 10m SLR and present day conditions in the ZUNO+ model. **c** Wave direction [^{o}] calculated from wave scenarios in the ZUNO+ model, for 10m SLR (magenta arrows) and present day conditions(black arrows) **d** Difference in root mean square orbital velocity near the bottom [ms^{-1}] calculated from wave scenarios, between 10m SLR and present day conditions in the ZUNO+ model.